

# Hierarchical micro-adaptation of biological structures by mechanical stimuli

P. Sáez<sup>b,c,\*</sup>, E. Peña<sup>b,c</sup>, M. Doblaré<sup>a,c</sup>, M.A. Martínez<sup>b,c</sup>

<sup>a</sup>*Group of Structural Mechanics and Materials Modeling. Aragón Institute of Engineering Research (I3A), University of Zaragoza, Zaragoza, Spain*

<sup>b</sup>*Applied mechanics and Bioengineering. Aragón Institute of Engineering Research (I3A), University of Zaragoza, Zaragoza, Spain*

<sup>c</sup>*CIBER-BBN. Centro de Investigación Biomédica en Red en Bioingeniería, Biomateriales y Nanomedicina.*

---

## Abstract

The objective of this work is to develop a remodeling model for biological matter coupling two different processes in a 3D framework: reorientation of the preferential direction of a given fibered structure and reorientation of the fibrils or filaments that make up such a structure. This work uses the microsphere-based approach to take into account the micro mechanics involved in biological fibered structures regarding both their passive behavior and the reorientation of their micro constituents. Moreover, the macro behavior of the material as a whole is obtained by means of homogenizing the underlying micro response. We associate the orientation space of the integration directions to the physical space of microfibrils. To approximate the directional distribution of the fibrils within each fiber bundle, a Bingham probability orientation density function is introduced into the Helmholtz energy function. With all these assumptions, the problem is studied from an energetic point of view, describing the dissipation inherent to remodeling processes, and the evolution equations for both reorientations (change in preferential direction of the network and change in shape of the fibril distribution) are obtained. The model is included in a finite element code which allows computing different geometries and boundary value problems. This results in a complete methodology for characterizing the reorientation evolution of different fibered biological structures, such as cells. Our results show remodeling of fibered structures in two different scales, presenting a qualitatively good agreement with experimental findings

in cell mechanics. Hierarchical structures align in the direction of the maximum principal direction of the considered stimulus and narrow in the perpendicular direction. The dissipation rates follows predictable trends although there are no experimental findings to date for comparison. The incorporation of metabolic processes and an insight into cell-oriented mechano-sensing processes can help to overcome the limitations involved.

*Keywords:* Remodeling, microsphere, biological tissue, cells, hyperelasticity, anisotropy

---

## 1. Introduction

Remodeling and other evolving processes such as growth or morphogenesis are key factors in the evolution of biological tissue in response to both external and internal epigenetic stimuli. Based on the description of these processes provided by Taber (1995) and Humphrey and Rajagopal (2002) for three important adaptation processes, remodeling, morphogenesis and growth (positive and negative), we shall consider the latter as the increase/decrease of mass via the increase/decrease of the number or size of cells, leading to a change in the volume of the organ. The work of Rodriguez et al. (1994) used the concept of natural configuration previously introduced by Skalak et al. (1982) to formulate volumetric growth. Later, Humphrey and Rajagopal (2002) proposed a constrained-mixture theory where changes in the density and mass of different constituents were taken into account. Many other works about biological growth have been presented in recent years, see e.g. Imatani and Maugin (2002); Garikipati et al. (2004); Gleason and Humphrey (2004); Menzel (2004); Ben Amar and Goriely (2005); Ganghoffer and Haussy (2005); Ateshian (2007); Goriely and Ben Amar (2007); Kuhl et al. (2007); Ganghoffer (2010a,b); Goktepe et al. (2010). Morphogenesis is associated to changes in the structure shape (Taber, 1995, 2009) while remodeling denotes changes in the tissue microstructure via the reorganization of the existing constituents or the synthesis of new ones with negligible volume change. All these processes involve changes in

---

\*Corresponding author at: Phone: (+34) 976.876555252; Fax: 976.762578

*Email address:* psaez@unizar.es (P. Sáez), miguelam@unizar.es (M.A. Martínez) (M.A. Martínez)

material properties. Although remodeling and growth can, and usually do, occur simultaneously, there are some cases where these processes develop in a decoupled way. For example, Stopak and Harris (1982) reported some experimental results showing remodeling driven by fibroblasts, with no volume growth. We will assume this scenario in this contribution, focusing exclusively on remodeling processes and on the reorientation of fibered biological structures.

It is well known that biological tissue remodels itself when driven by a given stimulus, e.g. mechanical loads such as an increase in blood pressure, or changes in the chemical environment that control the signaling processes and the overall evolution of the tissue. Biological remodeling can occur in any kind of biological tissue. In particular, the study of collagen as the most important substance to be remodeled, in all its types (preferentially Type I and III), has attracted considerable attention in recent years (Kuhl et al., 2005; Driessen et al., 2008; Machyshyn et al., 2010a,b). Collagen is considered the main bearing structure in many tissues, such as ligaments, tendons, arteries, etc. Collagen molecules are made up of three chains ( $\alpha$ -chains) coiled up in a helical-like structure. These molecules join in the extracellular matrix, creating collagen fibrils that are again assembled into larger collagen fibers (see e.g. the work of Fung (1990) for a general overview). The reorientation of this kind of structure can be assumed to be the consequence of the reorientation of the fibrils or filaments that make them up. This phenomenon leads to changes in the micro-structural orientation and fiber shape due to the reorientation of the fibrils (see e.g. Stopak and Harris (1982); Sander et al. (2009)). Several remodeling models have been proposed in recent years. Some of them analyze the reorientation of unidimensional fibers driven by different stimuli such as Menzel (2007) or Karsaj et al. (2009). Garikipati et al. (2006) presented an elegant energetic study of the remodeling problem from a thermodynamic point of view. Narayanan et al. (2010) presented a study dealing with the energy rates in growing tumors.

Another important biological structure able to remodel itself is the cell cytoskeleton. The cytoskeleton is composed of microtubules, microfilaments and a network of actin filaments, among many other elements (see e.g the review of Mofrad and Kamm (2006) and references therein for details). Cells move and reorient their inner structure depending on the stiffness

and strain of the substrate (Discher et al., 2005; De et al., 2007). The cytoskeleton shape can change by means of the adaptation of the microtubules and filaments in response to a specific external mechano-chemical stimulus (Saez et al., 2005; De et al., 2008). There are several experimental tests reported in the literature showing morphological changes in cells, resulting from mechanical stimulation of the matrix where the cells are located. There are two main procedures which induce morphological changes in cells, static and cyclic loading (De et al., 2007; De and Safran, 2008; Goli-Malekabadi et al., 2011). While static and low-frequency loading lead to reorientation and remodeling of the cellular structure parallel to the stretching direction (Collinsworth et al., 2000; Bischofs and Schwarz, 2003), cells in high-frequency cyclic tests align perpendicular to the loading direction. (Hayakawa et al., 2001; Jungbauer et al., 2008; Hsu et al., 2009; Faust et al., 2011; Chen et al., 2012). In the case of a high-frequency stimulus, the mechanosensing elements, the focal adhesions, are not able to follow such a quick changes and neither stress fibers nor miosin motors get activated. However, in static and low-frequency load states, focal adhesions react to such changes by means of an active internal tension of the stress fibers leading to changes in their morphology. These experimental results are characterized by a gradual reorientation of the principal direction of the cell followed by a progressive remodeling of the micro-structure leading to a narrower shape, see e.g. the experimental work of Dai et al. (2004) and the references therein. In Fig. 1 we show some results presented by Hayakawa et al. (2001) illustrating this behavior. In many cases this change of shape, unlike changes in orientation, is measured only by a shape-index Levesque et al. (1986); Galbraith et al. (1998); Farcas et al. (2009). The underlying biological processes, such as the dynamics of focal adhesions or the tension exerted by molecular motors over actin stress fibers are much more complex (see e.g. Mofrad and Kamm (2006) for an overall understanding of cell behavior). There are not many works describing these features of the inner structure. In terms of the orientation of the preferential direction of the cell, some of the most widely accepted models are those presented in De et al. (2007) and De and Safran (2008). The reorientation is assumed to be controlled by the matrix behavior and the forces that arise from the active regulation of the cell in a dipole-like manner. In terms of modeling changes in cell morphology due to

external stimuli, there are few models described in the literature, see e.g. Levesque et al. (1986); Ingber (2003); Ohashi and Sato (2005).

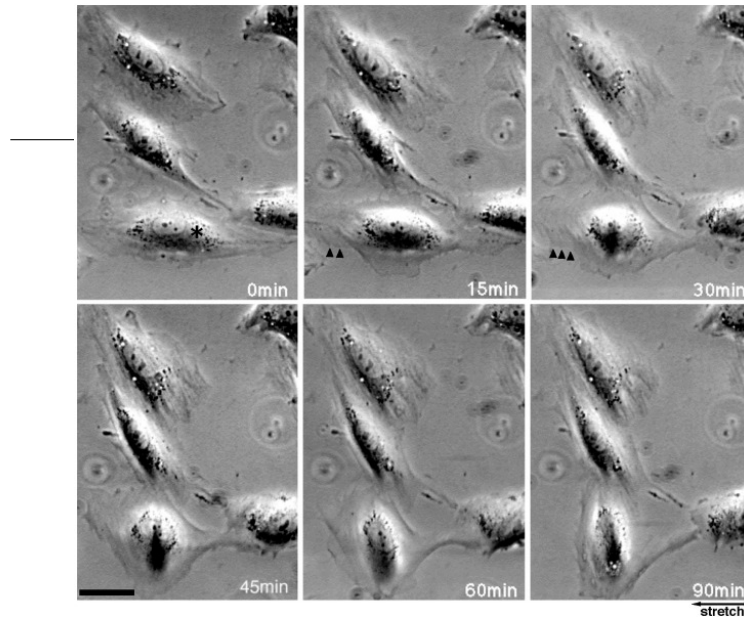


Figure 1: Results presented by Hayakawa et al. (2001) (with permission). Hayakawa and coworkers stretched cells cyclically over 90 minutes. Two different processes are observed, a reorientation of the mean direction of the cell and a morphological change in the cells due to adaptation of the internal cell elements, such as microtubules and stress fibers. A narrowed shape of the cell is obtained at the end of the experiment while the reorientation of the mean direction is detected at the beginning of the test.

Introducing multi-scale techniques is a straightforward approach to take into account underlying evolving processes. The works of Ingber (2008) about tensegrity models of cell structures is a good example in the field of cell mechanics. Miehe et al. (2004) performed a microsphere-based approach to study the microstructural behavior of polymers. Later, Caner and Carol (2006) applied this approach, also known as microplane, to vascular tissue. Microplane models were first used by Bazant and Oh (1985); Kuhl et al. (2000); Carol et al. (2004), among others, for studying the failure and plasticity of brittle materials, and they were later extended to other fields. Alastrué et al. (2009a) used this approximation to model vascular tissue including anisotropy. To gain a deeper insight into the underlying changes in the microstructure, some authors have included information about the dispersion

around the main orientation direction by using several statistical distributions. The von Mises distribution was introduced by Gasser et al. (2006) in the vascular framework to account for dispersion. Later Alastrué et al. (2010) used a Bingham distribution function (Bingham, 1974) to include the dispersion of the bundles and presented a comparison of these two statistical functions. In this context, some works (Menzel, 2007; Kroon, 2010; Grytz and Meschke, 2010) have included these statistical functions to account for remodeling. In multiscale homogenization schemes the macroscopic behavior is recovered by averaging the microstructural behavior represented, in the case of biological fibered tissue, by the mechanics of the fibrils or filaments. Previous authors (Alastrué et al., 2010) have used exponential-type models, such as that proposed by Holzapfel et al. (2000). Recently Menzel and Waffenschmidt (2009) presented a microsphere-based approach for remodeling, where the fibrils behavior was modeled by the Worm-like Chain model (WLC). WLC models have been extensively used for analyzing the behavior of the DNA double helix (see e.g. Bustamante et al. (2003)) and by Arruda and Boyce (1993) and Kuhl et al. (2005) to simulate elastomer and soft tissue respectively. Arruda and Boyce (1993) introduced this model in a non-affine isotropic eight chain model that has also been used by Bischoff et al. (2002). Garikipati et al. (2004) and Kuhl et al. (2005) extended it to anisotropic behavior. Alastrué et al. (2009a) and Alastrué et al. (2010) presented a comparison of both fibril models (exponential and WLC) in a microsphere-based approach. Note that along with the classical point of view of space orientations for microsphere-based models, we also associate the orientations to a physical orientation space of micro-structural elements, e.g., collagen fibrils in collagen bundles or microtubules and actin filaments in cells.

In short, we present a new remodeling model in 3D taking into account the reorientation of the mean direction of a given fibered structure and the reorientation of the individual fibrils or filaments leading to changes in the parameters of the associated probability orientation density function. In Section 2 we begin by discussing the material model used and in particular the WLC model adopted for each fibril. Later in this section, we present the Bingham statistical distribution, its main properties and general shape. We make use of the microsphere-based approach as a homogenization technique to move from the micro to the

macro-scale as described in the last part of Section 2. In Section 3, the evolution equations for remodeling are presented. We continue in Section 4 with the thermodynamical formulation of the problem obtaining the expression for the dissipation. The particularization of the model for the biological case is addressed in Section 5. In Section 6 we discuss some analytical examples to show the capabilities of our approach and in Section 7 we include our model in a finite element framework. We finish with a discussion of the advantages and limitations of the present contribution in Section 8.

## 2. Material model: Background Mechanics.

Our model is developed within a hyperelastic framework under a large strain hypothesis. The aim of this section is to introduce the strain energy density function (SEDF) for fibered structures, for example, materials with bundles of collagen fibrils or the cell cytoskeleton that will be used in this work. The main idea is to include microstructural information capable of reproducing the mechanical behavior and the shape of the spatial distribution of fibered constituents. A statistical distribution is considered to take into account the dispersion of the fibrils around a preferential orientation. Each fibril will be modeled by an individual strain energy function at the micro-level represented by the WLC model. We will finish this section with an academic example showing the mechanical behavior of the model and some simple examples of the passive mechanical behavior.

### 2.1. Non-linear continuum mechanics framework at large strains

For the kinematic of the problem we make use of the configuration changes of a given body  $\beta$ . Let  $\mathbf{X} \in \Omega_0$  be a particle in the reference configuration,  $\Omega_0 \subset \mathbb{R}^3$ , and  $\mathbf{x} \in \Omega$  the same particle in the spatial configuration  $\Omega \subset \mathbb{R}^3$ . The non-linear mapping that relates both configurations is denoted by  $\varphi : \Omega_0 \rightarrow \mathbb{R}^3$  and the associated linear tangent map, known as the deformation gradient,  $\mathbf{F} = \nabla_{\mathbf{x}}\varphi$  transforms tangent vectors from the material curves to spatial curves. We will restrict ourselves to a Cartesian metric.

Moreover, the deformation gradient and the Cauchy-Green strain tensor  $\mathbf{C}$  may be writ-

ten in decoupled form as in (Flory, 1961), namely

$$\mathbf{F} = J^{1/3}\bar{\mathbf{F}}, \quad \mathbf{C} = J^{2/3}\bar{\mathbf{C}} \quad (1)$$

where  $J = \det(\mathbf{F})$ , and  $\bar{\mathbf{F}}$  and  $\bar{\mathbf{C}}$  are the isochoric parts of the deformation gradient and Cauchy-Green tensor, respectively.

As is usual in the continuum mechanics of biological tissue, we will use a strain energy density function (SEDF) related to the mechanical contribution in a decoupled form, given by the volumetric and isochoric parts. The latter is decoupled again into isotropic and anisotropic parts as shown in Eq. 2.

$$\Psi_{\text{mech}} = \Psi_{\text{vol}} + \Psi_{\text{iso}} + \Psi_{\text{ani}} \quad (2)$$

where  $\Psi_{\text{vol}}(J)$  describes the SEDF associated to changes in volume,  $\Psi_{\text{iso}}(\bar{\mathbf{I}}_1, \bar{\mathbf{I}}_2)$  is the isotropic contribution to the isochoric deformation, with  $\bar{\mathbf{I}}_1 = \text{tr}(\bar{\mathbf{C}})$  and  $\bar{\mathbf{I}}_2 = 1/2[[\text{tr}(\bar{\mathbf{C}})]^2 - \text{tr}(\bar{\mathbf{C}}^2)]$ , usually related to the ground substance surrounding the fibers and described by a Mooney-Rivlin model. The isochoric anisotropic part  $\Psi_{\text{ani}}$  will be developed in the following sections.

## 2.2. Micro-sphere-based anisotropic approach

The microsphere-based model, also known as the micro-plane model, constitutes a homogenization technique that has been used previously for brittle materials (Bazant and Prat, 1988), damage and fracture (Bazant and Oh, 1985; Carol et al., 2001; Kuhl et al., 2001), polymers (Miehe et al., 2004) and biological tissue (Caner and Carol, 2006; Alastrué et al., 2009a), among many other applications. The homogenization or continuous averaging  $\langle\langle \bullet \rangle\rangle$  of a given variable  $(\bullet)$  is carried out by integrating over the unit sphere surface (Bažant and Oh, 1986; Heo and Xu, 2001). In order to perform a numerical implementation, the integral is computed by summing up the integrand over  $m$  discrete orientation vectors with the corresponding weight factors  $w^i$  as

$$\langle\langle \bullet \rangle\rangle = \frac{1}{4\pi} \int_{\mathbb{U}^2} (\bullet) dA \approx \sum_{i=1}^m w^i (\bullet)_i, \quad (3)$$

where  $dA$  is the differential area element of the unit sphere that may be written in terms of the spherical angles  $\alpha \in [0, \pi)$  and  $\phi \in [0, 2\pi)$  as  $dA = \sin(\alpha)d\phi d\alpha$ . The normalizing

term  $4\pi$  is the unit sphere total area  $A_{\mathbb{U}^2} = 4\pi$ . Although the microsphere approach was initially conceived and used as a multi-scale homogenization technique, each unidirectional integration direction can be interpreted as the contribution of the fibrils weighted by the  $dA$  associated to each direction. The contribution of the fibers to the SEDF may then be homogenized over the whole set of dimensions as (we refer to Miehe et al. (2004) for a review of these equations):

$$\Psi_{\text{ani}} = \frac{1}{4\pi} \int_{\mathbb{U}^2} \rho \psi(\bar{\lambda}) dA \approx \sum_{i=1}^m \rho_i w^i \psi(\bar{\lambda}_i), \quad (4)$$

where,  $\Psi_{\text{ani}}$  and  $\psi$  are the energy density functions in the macro and micro levels respectively,  $\rho$  is the statistical distribution with  $\rho_i$  the discrete value associated to each integration direction that includes the anisotropic behavior, and  $\bar{\lambda}_i$  is the stretch ratio for each integration direction  $\mathbf{r}^i$ .

### 2.3. Behavior of the fibrils

At the micro scale, we chose the well-established WLC model (Kratky and Porod, 1949) to define the SEDF for every fibril or filament. The WLC was used in DNA modeling by Bustamante et al. (2003). Subsequently it was used by Garikipati et al. (2005), Kuhl et al. (2005) and Alastrué et al. (2009a), among others, to model the behavior of biological tissue, extending the WLC molecular model to cover continuum tissue. Following this model, the individual contribution of each fibril or filament  $\psi(\bar{\lambda}_i)$  to the overall SEDF can be written as:

$$\psi(\bar{\lambda}_i) = \begin{cases} 0 & \text{if } \bar{\lambda}_i < 1 \\ \frac{n k \Theta}{4 A} \underbrace{\left[ 2 \frac{\bar{r}_i^2}{L} + \frac{L}{1 - \bar{r}_i/L} - \bar{r}_i - \ln(\bar{\lambda}_i^4 r_0^2) \right]}_{\psi_{chn}} \underbrace{\left[ \frac{1}{L} + \frac{1}{4 r_0 [1 - r_0/L]^2} - \frac{1}{4 r_0} \right]}_{\psi_{rep}} & \text{if } \bar{\lambda}_i \geq 1 \end{cases} \quad (5)$$

with  $n$  being the chain number density,  $k = 1.381 \times 10^{-23} (J/K)$  the Boltzmann constant and  $\Theta$  the absolute temperature, e.g.  $\Theta = 310K$  for biological tissue. The parameter  $A$  represents the persistence length (ratio between bending stiffness and thermal energy) and

$L$  the contour length.  $\bar{\lambda}_i = [\mathbf{r}_i \cdot \bar{\mathbf{C}} \cdot \mathbf{r}_i]^{1/2}$  is the stretch of each fibril,  $\bar{r}_i = \bar{\lambda}_i r_0$  and  $r_0$  the initial end-to-end length. Note that, as discussed in Section 2.1, the behavior of the fibered structure is related to the anisotropic part of the SEDF. The contribution  $\psi_{chn}$  is due to individual chains, while the repulsive term  $\psi_{rep}$  is introduced to preserve zero initial stresses in the reference configuration (unit stretches) driven by the non-vanishing initial length  $r_0$ . Note that this term can be modified to obtain residual stresses in the reference configuration, although we have not included this modification in the present work. Note that fibers are assumed not to bear any load under compression. We can obtain the stress tensors from Eq. 5 and write the deviatoric part of the Piola-Kirchoff,  $\bar{\mathbf{S}}_i = 2\partial_{\bar{\mathbf{C}}}\psi(\bar{\lambda}_i)$ .

#### 2.4. The Bingham probability distribution

A more realistic behavior of the fibered structure can be obtained by considering a statistical distribution of the fibrils to reflect the anisotropic response. We chose the Bingham orientation density distribution (Bingham, 1974) that provides more flexibility in modeling the dispersion of the fibrils than other commonly used distributions (Gasser et al., 2006; Alastrué et al., 2009a; Menzel et al., 2008). The Bingham distribution was previously used by Alastrué et al. (2010) to simulate the behavior of arterial tissue and may be expressed as

$$\rho(\mathbf{r}; \mathbf{Z}, \mathbf{Q}) = [F_{000}(\mathbf{Z}, \mathbf{r})]^{-1} \text{etr}(\mathbf{Z} \cdot \mathbf{Q}^T \cdot \mathbf{r} \cdot \mathbf{r}^T \cdot \mathbf{Q}), \quad (6)$$

where  $\mathbb{U}^2$  represents the unit sphere, and  $\mathbf{r} \in \mathbb{U}^2$  are director vectors,  $\text{etr}(\bullet) \equiv \exp(\text{tr}(\bullet))$ . The probability concentration is controlled by the eigenvalues of the diagonal matrix  $\mathbf{Z}$ ,  $\kappa_{1,2,3}$ , which may be interpreted as concentration parameters. In fact, the difference between the pairs  $[\kappa_1 - \kappa_2]$ ,  $[\kappa_1 - \kappa_3]$  and  $[\kappa_2 - \kappa_3]$  controls the shape of the statistical distribution over the unit sphere and, therefore, the concentration in the 3D space. For example, equal values of all the three parameters lead to an isotropic distribution of the probability while two values equal to zero represent a unidimensional distribution..  $\mathbf{Q} \in \text{SO}(3)$  represents the orthogonal local base that defines the directions of the statistical function.  $F_{000}(\mathbf{Z}, \mathbf{r})$  may be written as

$$F_{000}(\mathbf{Z}, \mathbf{r}) = [4\pi]^{-1} \int_{\mathbb{U}^2} \text{etr}(\mathbf{Z} \cdot \mathbf{r} \cdot \mathbf{r}^T) dA. \quad (7)$$

In our approach,  $\mathbf{Q}$  evolves to control the reorientation process of the maximal probability direction while  $\mathbf{r}$  also evolves changing, explicitly, the concentration of the Bingham orientation distribution without loss of generality. For the sake of simplicity we will consider the maximal probability direction of the orientation distribution function (ODF) to be initially oriented along  $\mathbf{Q}_{i,3}$  for  $i = 1, 2, 3$  with  $\kappa_3 \geq \kappa_2$  and  $\kappa_1 = 0.0$ . Figure 2 shows different shapes of the Bingham distribution for different values of  $\kappa_{1,2,3}$ .

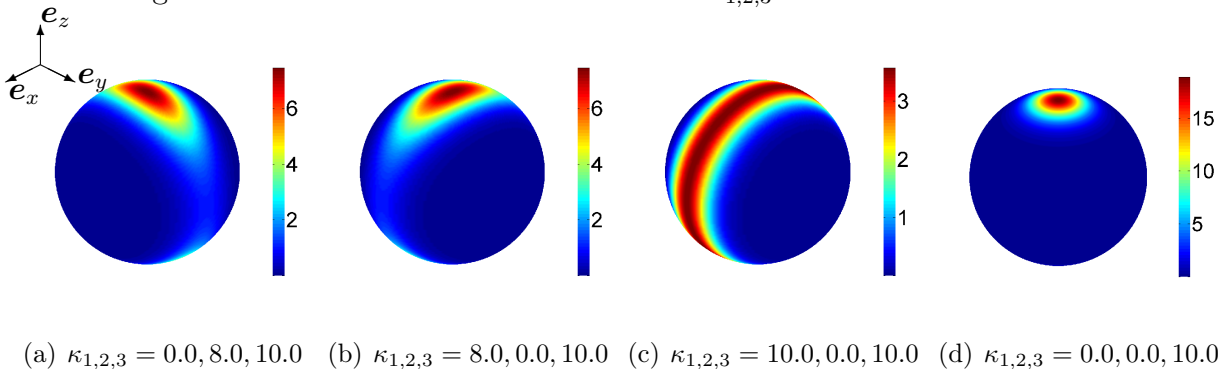
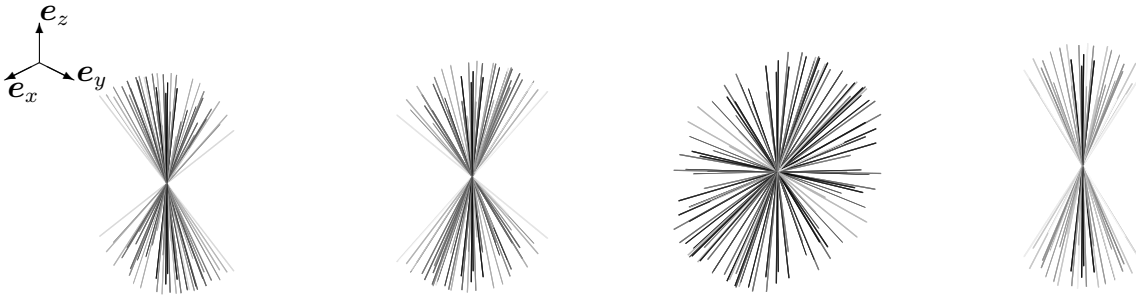


Figure 2: Shapes of the Bingham ODF and probability density values for different values of  $\kappa_{1,2,3}$  and  $\mathbf{Q} = \mathbf{e}_x \otimes \mathbf{e}_x + \mathbf{e}_y \otimes \mathbf{e}_y + \mathbf{e}_z \otimes \mathbf{e}_z$ . (a) and (b) represent the same distribution shape but rotated  $90^\circ$ . (c) provides a planar-type distribution and (d) presents a von Mises distribution, which can be considered as a particularization of the Bingham ODF.

The similarities between the structures in collagen bundles and cytoskeleton cells, and the discretization of the ODF over the unit sphere (Fig. 3) justify this approach. This assumption leads to a more real representation of the fiber distribution, as shown in Fig. 3, which corresponds to the functions depicted in Fig. 2. The fibrils distribution is represented weighted by the associated  $\rho$  in a gray scale, which will be discussed in detail below. At this point we would like to point out again that the classical assumption of an orientation space, as dealt with by microsphere-based models, is extended in our model to associate these vectors with fibrils of a fibered structure in a 3D space. We call this 3D space a physical space in contrast to the orientation space of the integration scheme.



(a) Fibril representation for  $\kappa_{1,2,3} = 0.0, 8.0, 10.0$  (Fig. 2(a))  
 (b) Fibril representation for  $\kappa_{1,2,3} = 8.0, 0.0, 10.0$  (Fig. 2(b))  
 (c) Fibril representation for  $\kappa_{1,2,3} = 10.0, 0.0, 10.0$  (Fig. 2(c))  
 (d) Fibril representation for  $\kappa_{1,2,3} = 0.0, 0.0, 10.0$  (Fig. 2(d))

Figure 3: Representation of the fibrils within the fibered structure for the Bingham ODF represented in Fig 2.

### 3. Evolution equations

As explained above, remodeling is controlled through two decoupled phenomena: first, the evolution of the orthogonal tensor  $\mathbf{Q}$ , which determines the rotation of the preferential directions and second the reorientation of the fibrils or filaments that changes the shape and parameters of the Bingham distribution. These processes can be identified in nature, e.g. those processes discussed in the introduction section such as rotations of cells in a dipole-like manner and the morphological changes. We base our evolution equations on the reorientation process described by Menzel (2004). The realignment will be driven by a given general stimulus characterized by a second order tensor.

#### 3.1. Preferential direction reorientation (PDR)

In this section we describe the reorientation of the whole fibered structure, given as the reorientation of the principal direction. The tensor  $\mathbf{Q} \in \text{SO}(3)$ , from where the orientation of the Bingham is defined, will evolve toward a new base defined by the eigenvectors of the driving stimulus  $\mathbf{\Xi}$ , denoted by  $\mathbf{\Xi}_I$ . We define a rotation tensor,  $\mathbf{R} \in \text{SO}(3)$ , as  $\mathbf{R} = \mathbf{\Xi} \cdot \mathbf{Q}^{-1}$  that takes into account the rotation of the orientation tensor of the Bingham distribution.. For the evolution of  $\mathbf{Q}$ , a geometrically exact update will be used. The Euler theorem states that "every element  $\mathbf{R} \in \text{SO}(3)$ , with  $\mathbf{R} \neq \mathbf{I}$ , is a rotation through an angle  $\theta = \|\boldsymbol{\omega}\|$  about an axis  $\boldsymbol{\omega}$ ", with  $\boldsymbol{\omega} \in \mathbb{R}^3$  being an eigenvector of  $\mathbf{R}$  with eigenvalue 1, that fulfills  $\mathbf{R}\boldsymbol{\omega} = \boldsymbol{\omega}$ .

$\mathbf{R}$  can be written in terms of the exponential mapping as  $\mathbf{R} = \exp(-\boldsymbol{\varepsilon} \cdot \boldsymbol{\omega})$  with  $\boldsymbol{\varepsilon}$  denoting the third-order permutation symbol. In short, it is possible to define a rotation vector  $\boldsymbol{\omega}$ , through which the initial base rotates to the final position (see Marsden and Ratiu (1999) for details). This approach follows that initially proposed by Menzel (2004) and Himpel et al. (2008) for one single fiber, Kuhl et al. (2005) for the eight-chain model and Karsaj et al. (2009) for 2D problems. From this, the rate of  $\mathbf{Q}$  is given by

$$\dot{\mathbf{Q}} = \hat{\mathbf{n}}^\omega \cdot \mathbf{Q}. \quad (8)$$

where  $\mathbf{n}^\omega = \boldsymbol{\omega}/\omega$ ,  $\omega = \|\boldsymbol{\omega}\|$  and  $\hat{\mathbf{n}}^\omega = -\boldsymbol{\varepsilon} \cdot \mathbf{n}^\omega$  are the norm of the angular velocity, its unit direction and the so called hat map of  $\boldsymbol{\omega}$ , respectively. For the temporal discretization, we consider a time interval  $\mathcal{T}$  and a number of subintervals,  $s$ ,  $\mathcal{T} = \bigcup_{n=0}^{s-1} [t^n, t^{n+1}]$  where the time increment is given by  $\Delta t = t^{n+1} - t^n$ . The evolution of the base at time  $n$  will evolve in the exponential mapping context as

$$\mathbf{Q}^{n+1} = \exp(-\boldsymbol{\varepsilon} \cdot \boldsymbol{\omega} \Delta t) \cdot \mathbf{Q}^n \quad (9)$$

which describes a rotation of the orientation at time  $n$ ,  $\mathbf{Q}^n$ , by the current rotation vector  $\boldsymbol{\omega}$  or the skew-symmetric tensor  $\hat{\boldsymbol{\omega}} = -\boldsymbol{\varepsilon} \cdot \boldsymbol{\omega}$ . Note that this approach follows an explicit updating scheme, with dependencies on the current position, different from the implicit scheme in Menzel (2004) where the updated quantities were obtained by means of Newton's iteration scheme. However, as Kuhl et al. (2005) pointed out, this is a reasonable approach for the gradual realignment followed herein. Note that for  $t \rightarrow \infty$ ,  $\mathbf{Q}^{n+1} \mapsto \boldsymbol{\Xi}$ . In order to compute the exponential map, this will be rewritten (see e.g. Marsden and Ratiu (1999)) by the Rodriguez formula, given  $\mathbf{R}(\boldsymbol{\omega})$ , as

$$\exp(\hat{\boldsymbol{\omega}}t) = [\sin(\|\boldsymbol{\omega}\|t)] \hat{\mathbf{n}}^\omega + [1 - \cos(\|\boldsymbol{\omega}\|t)] \mathbf{n}^\omega \otimes \mathbf{n}^\omega + \cos(\|\boldsymbol{\omega}\|t) \mathbf{I}, \quad (10)$$

### 3.2. Changes in the fibered structure shape. Reorientation of the fibrils (RF)

In this section we describe the reorientation model for the fibrils or filaments. Some authors have modeled this phenomenon by means of evolving statistical distributions (Driessen et al., 2008; Menzel et al., 2008). Menzel et al. (2008) studied this issue by using a von Mises

distribution and the evolution of the associated structural tensor. More recently Menzel and Waffenschmidt (2009) presented a work for remodeling within a microsphere approach, where from an initial isotropic state, the reorientation of each of the integration directions leads to an anisotropic behavior. This latter approach is similar to that described in Himpel et al. (2008) for one simple fiber, and it is the approach that we adopt for the reorientation of the microstructure.

In this work we make use of the Bingham distribution (see Section 2.4). Three different options for defining its rate are discussed. *(i)* Defining a rate of the diagonal tensor  $\mathbf{Z}$ . This approach has some disadvantages since the actual quantities that establish the function shape are the differences between the values of  $\mathbf{Z}$ , but not the values themselves. Therefore, it is not trivial to obtain an evolution equation that can be introduced consistently in the thermodynamic framework, which evolves correctly with any driven quantity and has a consistent physical interpretation. Moreover, this approach would introduce more phenomenological parameters. *(ii)* Defining second and fourth-order tensors following the developments described by Menzel et al. (2008). This approach also has some difficulties regarding the definition of a closed parameterized form. Computation of these parameters turns out to be a complex task (see Menzel et al. (2008) for additional details of this procedure), and this is not the goal of this contribution. *(iii)* Definition of the rate equation for each integration direction to be reoriented. This procedure was initially proposed by Menzel and Waffenschmidt (2009) and is the approach adopted herein. Moreover, with such an approach, we are able to evolve the shape of the microstructure by means of the evolution of each integral direction. From our point of view, this approach allows a free reorientation of the fibrils since they are not limited by the statistical distribution.

It is necessary to define the vector  $\boldsymbol{\omega}_i$ , which leads the evolution of the reorientation process. As mentioned above, we prefer to generalize the driving quantity leading the process, named  $\boldsymbol{\Xi}$ . We assume that the realignment depends on the maximum principal direction of  $\boldsymbol{\Xi}$ , such that  $\mathbf{r}_i \mapsto \boldsymbol{\Xi}_3$ . We will denote by  $I = 1, 2, 3$  the eigenvectors associated to the minimum, medium and maximum eigenvalues of  $\boldsymbol{\Xi}$ , respectively. This leads to

$$\boldsymbol{\omega}_i := \mathbf{r}_i \times \boldsymbol{\Xi}_3 \tag{11}$$

where  $\boldsymbol{\omega}_i$  and  $\mathbf{r}_i$  are the angular velocity and the unit vector of each integration direction as depicted in Fig. 4. We will again make use of the updating scheme presented in the section above, based on the exponential map, and again adopt an explicit updating. Therefore, we approximate the updated vector as

$$\mathbf{r}_i^{n+1} = \exp(\hat{\boldsymbol{\omega}}_i \Delta t) \cdot \mathbf{r}_i^n \quad (12)$$

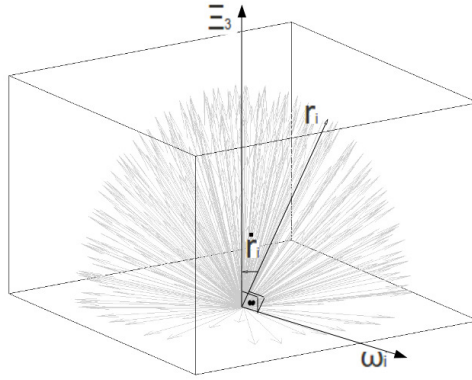


Figure 4: Evolution of each integration direction.

**Remark 1.** *Reconstruction of the Bingham distribution from the reoriented integration directions.* Once the integration directions evolve, it is obvious that the distribution of the fibrils changes independently of the initial Bingham ODF, but it is not so clear how the values of  $\mathbf{Z}$  change. In order to recover a Bingham distribution, mainly for visualization purposes we adopt the following methodology. Given an updated state, after reorientation of the integration directions (ID) at the current time  $n$ :

- We define a structural tensor  $\boldsymbol{\rho}$  at time  $n$  as

$$\boldsymbol{\rho}^n = \frac{1}{4\pi} \int_{\mathbb{U}^2} \rho(\mathbf{r}^n; \mathbf{Z}, \mathbf{Q}^n) \mathbf{r}^n \otimes \mathbf{r}^n d\mathbf{A} \quad (13)$$

- At this point we can follow two options:
  - i) We solve the non-linear equation system (Eq. 14) obtaining the new values of  $\mathbf{Z}$ ,

named  $\hat{\mathbf{Z}}$ , from the right side of the equality.

$$\frac{1}{4\pi} \int_{\mathbb{U}^2} \rho(\mathbf{r}^n; \mathbf{Z}, \mathbf{Q}^n) \mathbf{r}^n \otimes \mathbf{r}^n dA = \frac{1}{4\pi} \int_{\mathbb{U}^2} \rho(\mathbf{r}; \hat{\mathbf{Z}}, \mathbf{Q}) \mathbf{r} \otimes \mathbf{r} dA. \quad (14)$$

*ii)* We can construct a data base with pairs of data relating the values of each  $\rho^n$  with its respective  $\mathbf{Z}$  tensor. We followed this latter method for  $\kappa_{1,2,3} = 1 \dots 100$ , leading to a database of  $10^6 \times 3$  elements for  $\kappa$  and  $10^6 \times 3$  elements for the diagonal components of  $\rho$ .

#### 4. Dissipation

The starting point of this section arises from the first and second laws of thermodynamics given in the material description, which may be written as:

$$\dot{e} = \mathbf{P} : \dot{\mathbf{F}} - \text{DIV} \hat{\mathbf{Q}} \quad \text{and} \quad \gamma = \dot{\eta} - \text{DIV} \frac{\hat{\mathbf{Q}}}{\theta}, \quad (15)$$

where  $\dot{e}$  is the internal energy rate of the system,  $\mathbf{P}$  the first Piola-Kirchoff stress,  $\hat{\mathbf{Q}}$  the heat flux,  $\eta$  the entropy density,  $\theta$  the absolute temperature and  $\gamma$  an entropy production term coming from irreversible processes (see e.g. Truesdell and Noll (2004)). Combining the Legendre transformation  $\Psi = e - \eta\theta$  in Eq. 15 with the Helmholtz free energy density  $\Psi$ , we can write the Clausius-Plank inequality as

$$\mathcal{D} = -\dot{\Psi} + \mathbf{P} : \dot{\mathbf{F}} + \frac{\hat{\mathbf{Q}} \cdot \text{DIV} \theta}{\theta} \geq 0 \quad (16)$$

where  $\mathcal{D} \geq 0$  is the internal dissipation or the local entropy production, also named  $\theta\gamma$ . This inequality has important implications in remodeling processes, since it is well known that this is an irreversible process and Eq. 16 is a strict inequality. Usually in mechanics, the last term is omitted since no thermal effects are considered. We do not omit it in this first description in order to have a more general formulation. We now split the Helmholtz free-energy function as  $\Psi = \Psi_{\text{mech}} + \Psi_{\text{chem}}$ . The mechanical part  $\Psi_{\text{mech}}$  refers to the classical energy used in non-linear mechanics and  $\Psi_{\text{chem}}$  to the chemical metabolic component. Although there is no argument that in biological tissue the exchange of energy through chemical processes is essential, obtaining  $\Psi_{\text{chem}}$  is complex and to the authors knowledge has not been sufficiently developed. Mechanical stimuli are not enough to boost remodeling

in biological tissue and metabolic processes are fundamental. In fact, chemical processes are responsible for initiating and leading the remodeling of biological tissue and cells, although sometimes mediated by mechanical mechanisms. Metabolic stimuli can arise from genetic or sympathetic disorders although they usually arise from a previous mechanical stimulus. This very first and final mechanical role in remodeling is the reason why we adopt a mechanical-based approximation of the problem. As previously mentioned, we will ignore heat sources and will only consider isothermal processes. Most biological tissue works and develops at approximately constant temperature so only the mechanical part will be considered. As observed above, the dependencies of the mechanical term lies in  $\Psi_{\text{mech}}^{\mathbf{F}} = \Psi_{\text{mech}}(\mathbf{F}, \mathbf{r}, \mathbf{Q})$  or, in terms of the right Cauchy-green tensor  $\mathbf{C}$ , in  $\Psi_{\text{mech}}^{\mathbf{C}} = \Psi_{\text{mech}}(\mathbf{C}, \mathbf{r}, \mathbf{Q})$ . Taking into account Eq. 2, and focusing on the anisotropic part, which is the contribution we assume reorients itself, we can define

$$\Psi_{\text{ani}} = \frac{1}{4\pi} \int_{\mathbb{U}^2} \rho(\mathbf{Q}, \mathbf{r}) \psi(\bar{\lambda}) dA, \quad (17)$$

with the material derivative

$$\dot{\Psi}_{\text{ani}} = \partial_{\mathbf{C}} \Psi_{\text{ani}} : \dot{\mathbf{C}} + \partial_{\mathbf{r}} \Psi_{\text{ani}} \cdot \dot{\mathbf{r}} + \partial_{\mathbf{Q}} \Psi_{\text{ani}} : \dot{\mathbf{Q}}. \quad (18)$$

From the first term we obtain the constitutive equation for the deviatoric part of the anisotropic stress as  $\mathbf{S}_{\text{ani}} = J^{-2/3} \text{DEV}(\bar{\mathbf{S}}_{\text{ani}})$ , where  $(\bar{\mathbf{S}}_{\text{ani}})$  is the fictitious second Piola-Kirchhoff stress tensor defined as

$$\bar{\mathbf{S}}_{\text{ani}} = \frac{1}{4\pi} \int_{\mathbb{U}^2} \rho \partial_{\mathbf{C}} \psi(\bar{\lambda}) dA = \frac{1}{4\pi} \int_{\mathbb{U}^2} \rho \bar{\lambda}^{-1} \psi'(\bar{\lambda}) \mathbf{r} \otimes \mathbf{r} dA. \quad (19)$$

The other two terms represent the dissipation due to the remodeling process, reducing the inequality to

$$\mathcal{D}_{\text{int}} = -\partial_{\mathbf{r}} \Psi_{\text{mech}} \cdot \dot{\mathbf{r}} - \partial_{\mathbf{Q}} \Psi_{\text{mech}} : \dot{\mathbf{Q}} = \underbrace{-\frac{1}{4\pi} \int_{\mathbb{U}^2} \psi \partial_{\mathbf{Q}} \rho : \dot{\mathbf{Q}} dA}_{\mathcal{D}_{\text{PDR}}} - \underbrace{\frac{1}{4\pi} \int_{\mathbb{U}^2} [\rho \partial_{\mathbf{r}} \psi + \psi \partial_{\mathbf{r}} \rho] \cdot \dot{\mathbf{r}} dA}_{\mathcal{D}_{\text{RF}}} \quad (20)$$

The first term is related to dissipation due to reorientation ( $\mathcal{D}_{\text{PDR}}$ ) of the principal direction of the bundle while the second term ( $\mathcal{D}_{\text{RF}}$ ) is caused by reorientation of the individual fibrils or filaments, which leads to a change in the bundle shape.

$$\mathcal{D}_{\text{PDR}} = -\frac{1}{4\pi} \int_{\mathbb{U}^2} [\psi \partial_{\mathbf{Q}} \rho : \dot{\mathbf{Q}}] dA = -\frac{1}{4\pi} \int_{\mathbb{U}^2} [2\mathbf{r} \cdot [\mathbf{r}^T \cdot \mathbf{Q} \cdot \mathbf{Z}] \rho \psi : \dot{\mathbf{Q}}] dA \quad \text{and} \quad (21)$$

$$\mathcal{D}_{\text{RF}} = -\frac{1}{4\pi} \int_{\mathbb{U}^2} [\rho \partial_{\mathbf{r}} \psi + \psi \partial_{\mathbf{r}} \rho] \cdot \dot{\mathbf{r}} dA = -\frac{1}{4\pi} \int_{\mathbb{U}^2} [S_i \bar{\mathbf{C}} \cdot \mathbf{r} \rho + \rho 2\mathbf{Q} \cdot \mathbf{Z} \cdot \mathbf{Q}^T \cdot \mathbf{r} \psi + \rho_m \psi] \cdot \dot{\mathbf{r}} dA, \quad (22)$$

with  $\partial_{\bar{\lambda}^2} \psi = S_i/2$ ,  $\partial_{\mathbf{r}} \bar{\lambda}^2 = 2\bar{\mathbf{C}} \cdot \mathbf{r}$  and

$$\rho_m = \left[ \int_{\mathbb{U}^2} [4\pi]^{-1} 2\mathbf{Z} \cdot \mathbf{r} \operatorname{etr}(\mathbf{Z} \cdot \mathbf{r} \cdot \mathbf{r}^T) dA \right]^{-1} \operatorname{etr}(\mathbf{Z} \cdot \mathbf{Q}^T \cdot \mathbf{r} \cdot \mathbf{r}^T \cdot \mathbf{Q}). \quad (23)$$

In subsequent sections we provide the dissipation values for several examples.

## 5. Particularization for biological tissue

The previous sections have omitted any reference to specific quantities that drive the remodeling process. In the following section we discuss some of the driving quantities most commonly used in the bibliography. Moreover, we also present a comparison of the behavior of the model with various previously proposed driving quantities.

As pointed out in the Introduction section, it is still unclear if this quantity is associated to strains, stresses or mix-variant types such as the Mandel tensor (see e.g. reviews in Humphrey (2001); Cowin (2004); De et al. (2007) and references therein). Kuhl et al. (2005) and Himpel et al. (2008) followed a strain based approach while Driessen et al. (2004) suggested the orientation along a direction between the two principal directions of maximum strain. Other authors (Kuhl and Holzapfel, 2007; Grytz and Meschke, 2010) suggested stress-based models to trigger the process, some of them aligned with the maximum principal direction or with respect to a direction between the two maximum principal directions. This option is frequently applied to cardiovascular tissue where the fibers remodel themselves to compensate for variations in both internal pressure and wall shear stress (Taber, 1998; Alford et al., 2008). Finally, other authors (Imatani and Maugin, 2002; Menzel et al., 2008) proposed a mix-variant Mandel-type tensor.

It is also worth commenting on the particular state reached when the strain and stress tensors are coaxial and a critical state of the free energy is achieved (Cowin, 1994; Vianello, 1996) in which case  $\mathbf{M} = \mathbf{C} \cdot \mathbf{S}$  turns out to be symmetric. Anisotropic materials are not coaxial in general and this state is only maintained while the Piola-Kirchhoff stresses and the Cauchy-Green tensor retain non-coaxiality.

Note also that our model is restricted to static or low frequency loads, or more precisely, to cases where the characteristic time of remodeling is shorter than the characteristic period of loads. As discussed in the introduction biological tissue and particularly cells, behave in different ways when they are stimulated statically or by cyclic loads.

The aim of this analysis is not to provide any new hypothesis or clarification about which quantity is the correct one, but to compare the evolution of the dissipation achieved with the three types of driving quantities described below. The whole process will be split into two steps.

### 5.1. Preferential direction reorientation

The first type corresponds to the reorientation of the preferential directions, defined by means of a rotation tensor  $\mathbf{Q}$  that will be driven by the principal Cauchy-Green strain directions ( $\Xi_I^C$ ), the principal Cauchy stresses ( $\Xi_I^S$ ) or the principal directions of the Mandel tensor ( $\Xi_I^M$ ). This does not uniquely define the evolution of  $\mathbf{Q}$ , so we have to enforce the preferential direction, that is the direction with the maximum fibril concentration, to reorient itself towards the maximum principal direction of the driving quantity  $\Xi$ . This description is not influenced by the magnitude of the driving stimulus but only by the angle between the initial and the goal directions. In order to overcome this limitation we introduce a magnitude-dependent parameter  $\zeta^\Xi$  as

$$\zeta^\Xi = \begin{cases} 0 & \text{if } \Lambda_3^\Xi/\Lambda_1^\Xi \leq \zeta_0^\Xi \\ \Lambda_3^\Xi/\Lambda_1^\Xi - \zeta_0^\Xi & \text{if } \Lambda_3^\Xi/\Lambda_1^\Xi > \zeta_0^\Xi \end{cases}, \quad (24)$$

where  $\Xi$  denotes the driving quantity ( $\mathbf{C}$ ,  $\mathbf{S}$  or  $\mathbf{M}$ ),  $\Lambda_3^\Xi/\Lambda_1^\Xi \in [1, \text{inf})$  the ratio between the maximum and minimum eigenvalues of the chosen driving quantity  $\Xi$ , and  $\zeta_0^\Xi$  a threshold value that sets the coefficient value at which the reorientation process starts. Besides the magnitude of the driving quantity, it seems reasonable to suppose that natural tissue adapts to a given load in different ways, e.g. collagen fibrils remodel in a different way than microtubules of a cell. We therefore introduce the last material parameter,  $\zeta_*^\Xi$ , that provides a measure of the particular tissue reorientation velocity, decreasing for higher reorientation

rates. We propose to fulfill  $\Delta t \zeta^{\Xi} / \zeta_*^{\Xi} \leq t^{n+1}$ , leading to the following updating scheme of Eq. 9

$$\mathbf{Q}^{n+1} = \exp(\zeta^{\Xi} \hat{\omega} \Delta t / \zeta_*^{\Xi}) \cdot \mathbf{Q}^n \quad (25)$$

### 5.2. Reorientation of the fibrils

The second step deals with the remodeling of the fibered structure which is basically, as discussed above, a reorientation of the fibrils or filaments that make up such a structure. The driving quantity will be the same and, again, we introduce a magnitude-dependent parameter  $\bar{\zeta}^{\Xi}$  and the corresponding material dependent parameter  $\bar{\zeta}_*^{\Xi}$ . We have adopted the same definition as in the reorientation process, being

$$\bar{\zeta}^{\Xi} = \begin{cases} 0 & \text{if } \Lambda_3^{\Xi} / \Lambda_1^{\Xi} \leq \bar{\zeta}_0^{\Xi} \\ \Lambda_3^{\Xi} / \Lambda_1^{\Xi} - \bar{\zeta}_0^{\Xi} & \text{if } \Lambda_3^{\Xi} / \Lambda_1^{\Xi} > \bar{\zeta}_0^{\Xi} \end{cases}, \quad (26)$$

with  $\bar{\zeta}_0^{\Xi}$  the value at which the remodeling starts. And again, the updating scheme of Eq. 12 changes to

$$\mathbf{r}^{n+1} = \exp(\bar{\zeta}^{\Xi} \hat{\omega}_i \Delta t / \bar{\zeta}_*^{\Xi}) \cdot \mathbf{r}^n \quad (27)$$

**Remark 2.** *Coupling of reorientation models.* The reorientation processes discussed above occur simultaneously in biological tissue, but in different ways. For example, the reorientation of the fibrils or filaments of the structure begins a certain time after the start of the reorientation of the whole structure and perhaps at different rates. However, there are no available experimental tests that clearly distinguish between both processes. Therefore, in order to show the capabilities of this model, and without loss of generality, we will assume in section 6 that the reorientation process occurs only when the preferential direction is aligned with the eigenvector associated to the maximum eigenvalue of the driving quantity. Upon the assumption of decoupled reorientations, we can set  $\bar{\zeta}_0^{\Xi}$  to  $\bar{\zeta}_0^{\Xi} \geq \max\{\Lambda_3^{\Xi} / \Lambda_1^{\Xi}\}$  achieved during the PDR process to allow for a smooth transition from one process to the other. In this way, we will consider them as decoupled in Section 6. However, for Section 7 a coupled evolution will be considered by a material parameter,  $\varsigma = 1 / [1 + \exp(\varsigma_c * [||\boldsymbol{\omega}||t - \varsigma_s])]$ . This

equation follows a sigmoidal function and the parameters  $\varsigma_c$  and  $\varsigma_s$  control the rotation value of the PDR at which RF begins and its rate, respectively.  $\varsigma$  multiplies the arguments of the exponential in Eq. 27.

Table 5 summarize the principal equations and the workflow of the model.

## 6. Results

### 6.1. Principal direction reorientation

The main features of the preferential direction reorientation model under discussion and some of the results obtained are presented in this section. We have chosen a homogeneous deformation problem controlled by displacement. We use the deformation gradient given by  $\mathbf{F} = 1/\sqrt{\lambda}\mathbf{e}_x \otimes \mathbf{e}_x + 1/\sqrt{\lambda}\mathbf{e}_y \otimes \mathbf{e}_y + \lambda\mathbf{e}_z \otimes \mathbf{e}_z$ , the set of concentration parameters  $\kappa_{1,2,3} = [0, 8, 10]$  and an initial  $\mathbf{Q} = \mathbf{e}_x \otimes \mathbf{e}_x + \mathbf{e}_z \otimes \mathbf{e}_y - \mathbf{e}_y \otimes \mathbf{e}_z$ , which places the preferential direction of the fibered structure perpendicular to the stretching direction. All these parameters have been chosen to show the behavior of the model and they have not been fitted from experimental data. The parameters from the WLC model are set to  $r_0 = 1$ ,  $L = 2$ ,  $A = 1.3$ ,  $n = 7.0 \times 10^{21}$ ,  $k = 1.381 \times 10^{-23} J/K$  and  $\theta = 300K$ . The Mooney-Rivlin parameters are  $C_1 = 1$  and  $C_2 = 0.2$ , in the same order of magnitude as those in Alastrué et al. (2009a) or Kuhl et al. (2005) representing parameter values of biological tissue such as arteries or skin. We present results for the three types of driving quantities analyzed ( $\mathbf{C}$ ,  $\mathbf{S}$  and  $\mathbf{M}$ ). The normalized time interval has been discretized in 100 time steps with  $\Delta t = 0.1$ .

We first analyzed the results without taking into account the biological model described in Section 5. In Fig. 5 we present the evolution of the tensor  $\mathbf{Q}$  every ten steps in a stereographic projection, used previously by Menzel and Steinmann (2003), among others, for plasticity and by Miehe et al. (2004) and by Alastrué et al. (2009a) to represent the stress in blood vessel fibers. The results show almost no difference between the updated positions of  $\mathbf{Q}$  for the three driving quantities. In the zoom shown in Fig 5(b) we see that the position driven by the Mandel tensor is placed between those driven by strain (closer to the goal position, and so faster) and stress (slower).

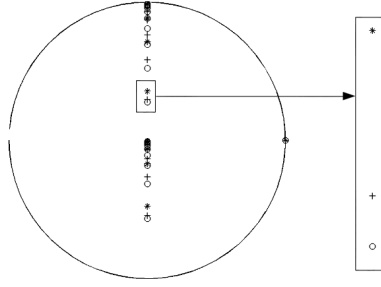


Figure 5: Evolution of  $\mathbf{Q}$ , plotted in a stereographic representation, driven by  $\mathbf{C}(o)$ ,  $\mathbf{S}(*)$  and  $\mathbf{M}(+)$ . The detail for time step 10 shows that the evolution driven by  $\mathbf{C}(o)$  reorient the fastest, followed by  $\mathbf{M}(+)$  and  $\mathbf{S}(*)$  as depicted in Fig.6 .

An alternative for visualizing the material evolution is computing an anisotropic measurement as proposed by Menzel and Steinmann (2003). In this way, we can measure how fast the reorientation is by means of the scalar  $\delta$ , or the anisotropic measure as

$$\delta(\mathbf{C}, \mathbf{S}) = \frac{\|\mathbf{C} \cdot \mathbf{S} - \mathbf{S} \cdot \mathbf{C}\|}{\|\mathbf{S}\| \|\mathbf{C}\|}. \quad (28)$$

$\delta(\mathbf{C}, \mathbf{S})$  vanishes at equilibrium. We represent the Cauchy stress evolution, anisotropy (given by Eq. 28) and dissipation in the present example. Fig. 6(a) shows that that the stress rises from about 12 kPa (stiffness of the extracellular matrix) up to 33 kPa due to the contribution of the bundle that progressively aligns with respect to the stretching direction. Fig. 6(b) shows the anisotropic measure evolution and Fig. 6(c) the dissipation evolution. We can observe that the difference is quite small. We impose a stopping criterion for rotation angles less than 0.01 degrees. For such an assumption we reach steps 49, 73 and 54 for the strain, stress and Mandel driven problem respectively. If we compute the dissipation numerically, we obtain from Eq. 21,  $\mathcal{D}_{\mathbf{C}} = 3.446 \times 10^2$  [kPa/time],  $\mathcal{D}_{\mathbf{S}} = 2.860 \times 10^2$  [kPa/time] and  $\mathcal{D}_{\mathbf{M}} = 3.303 \times 10^2$  [kPa/time] which established stress as the least dissipative quantity.

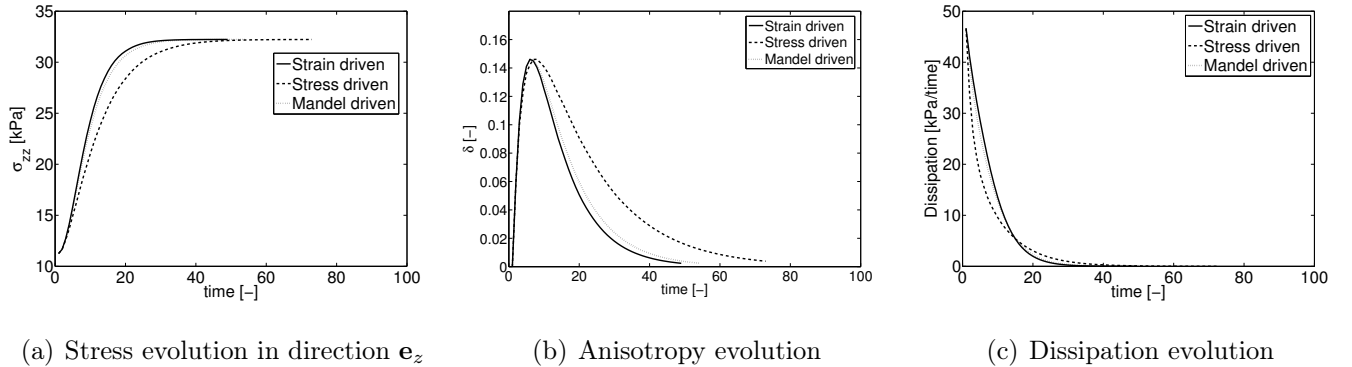


Figure 6: Evolution of stress, anisotropy and dissipation.

We check the last step in which the angle between the principal direction and the goal direction is less than  $0.01\text{rad}$ , which we consider to be the equilibrium situation. In Table 1 we show the equilibrium step for each driving quantity and for two fiber parameters for the WLC model, a softer one  $L= 2.0$ , and a stiffer one  $L= 1.8$ , and the rest of the parameters as set above. Note that the values of the contour length  $L$  close to  $r_0$  represent stiffer values than those much higher than  $r_0$ . The principal direction due to stresses has two components, one due to the isotropic part and another due to the anisotropic part, which correspond to the fibered structure. In a material with stiff fibers and not aligned with the direction of the load, the anisotropic contribution is more important and the principal direction do not fit in the direction of the load. Therefore, during the evolution process, the total maximum eigenvector moves toward the direction of the load. However, when the process is driven by strains, the goal direction maintain a constant direction and the equilibrium is achieved in the same time step for the two degrees of fiber stiffness.

Stiffer			Softer		
strain	stress	Mandel	strain	stress	Mandel
49	73	54	49	100	23

Table 1: Time step in which equilibrium is achieved for different fiber stiffness and different driving quantities.

**Remark 3.** *Stiffness material dependence.* The behavior of the reorientation process must

also be related to the ratio between the anisotropic and the isotropic part of the stiffness. To analyze this aspect we perform a simple case of a 1D fiber, placed initially perpendicular to the stretching direction and gradually moving towards the direction of the load. As we can see in Fig 7, the higher the matrix-stiffness/fiber-stiffness ratio, the faster the reorientation. This shows that for higher ratios, the principal stress value and the associated direction of the ground substance have greater relevance in the overall stress response. Besides, up to 23 degrees there is no anisotropy since the fibrils are under compression and, therefore, they do not contribute to stress. At this point, some fibrils begin to bear some load contributing to the anisotropic behavior of the material.

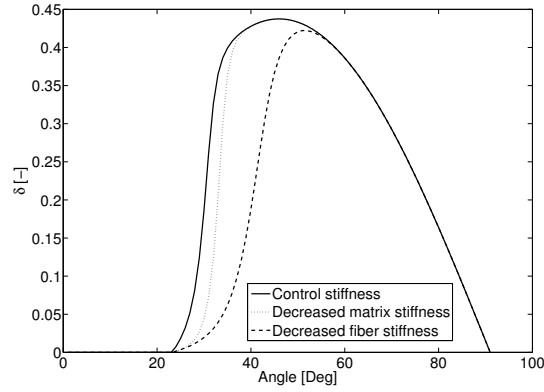
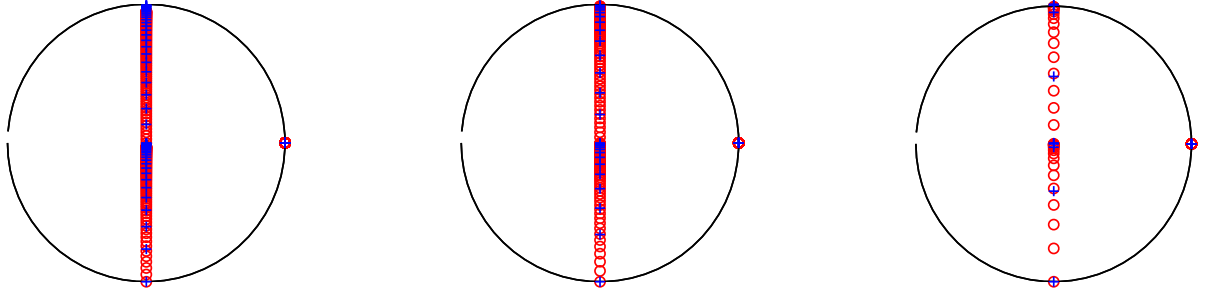


Figure 7: Evolution of anisotropy for a 1D fiber.

The particularization to biological tissue discussed in Section 5 is now included. We take into account the dependence on the magnitude of the load. With this aim we introduce in the remodeling approach the material parameters  $\zeta^{\Xi}$ ,  $\zeta_*^{\Xi}$  and  $\zeta_0^{\Xi}$  (fixed to 1 for strain driven and 0 for stress driven). We will study the model for  $\zeta_*^{\mathbf{n}} = 2, 10$ . Fig. 8 shows the situation of  $\mathbf{Q}$  at every step. Higher values of  $\zeta_*^{\Xi}$  lead to lower rates of evolution, as expected. The process driven by  $\mathbf{M}$  presents higher rates than those driven by stress, while the latter are higher than those driven by strain.



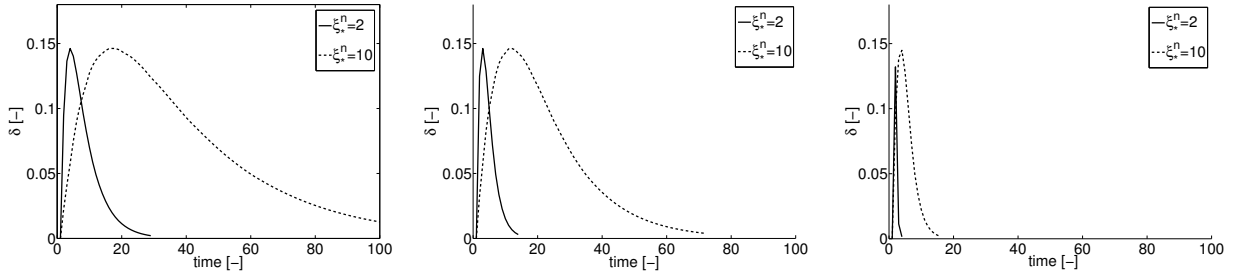
(a) Change with  $\mathbf{C}$

(b) Change with  $\mathbf{S}$

(c) Change with  $\mathbf{M}$

Figure 8: Evolution of  $\mathbf{Q}$  driven by different quantities. Blue crosses indicate the results for  $\zeta_*^{\Xi} = 2$  and red circles those for  $\zeta_*^{\Xi} = 10$ .

We also present the anisotropy evolution for each situation discussed above. As the previous results show, it can be seen that the preferential direction aligns more slowly with the principal direction with higher values of  $\zeta_*^{\Xi}$ . Table 2 shows the step at which we obtain a rotation of less than 0.01 degrees, which can be considered as the equilibrium situation.



(a) Change with  $\mathbf{C}$

(b) Change with  $\mathbf{S}$

(c) Change with  $\mathbf{M}$

Figure 9: Anisotropy measure  $\delta$  for the different driving quantities and  $\zeta_*^{\Xi} = 2$  and  $\zeta_*^{\Xi} = 10$ .

$\zeta_*^{\Xi} = 2$			$\zeta_*^{\Xi} = 10$		
strain	stress	Mandel	strain	stress	Mandel
29	14	4	>100	72	16

Table 2: Time step in which equilibrium is achieved for different driving quantities and material parameters  $\zeta_*^{\Xi} = 2$  and  $\zeta_*^{\Xi} = 10$ .

We present in Fig. 10 the dissipation evolution of the examples proposed in this section. Note that the scale in the vertical axes is modified in the different subfigures. Consistent with the previous results, the process driven by strain and higher values of  $\zeta_*^\Xi$  is the least dissipative and, therefore, the optimum from an energetic point of view. It should be noted that these results are obtained from the assumed biological parameters that should be experimentally validated and fitted to obtain realistic conclusions. We refer to the results shown in Fig. 6 where no material parameter has been included and therefore a clearer interpretation of the role of the different driving quantities can be achieved. As can be seen in Fig. 10, and more clearly in Table 3, the quantity that produces the least dissipation is strain, as mentioned above, followed by stress and Mandel respectively. Dissipation is also lower for higher values of  $\zeta_*^\Xi$ . Based on the Eq. (26) for the evolution of the orientation tensor the Bingham distribution, strain turn to be the least dissipative quantity because our magnitude-dependent parameter  $\xi^\Xi$  give us a lower value in the strain-driven case. This parameter multiply the rotation quantities in the exponential mapping leading to a slower evolution rate and a lower dissipation rate. This parameter weight the evolution rate, as we explain after Eq. (25), in terms of the coefficient of the maximum and minimum eigenvalues. While the strain-based case give relatively small coefficients, stress-driven problems are much more material-dependent and this coefficient turn to be higher.

Finally we present the evolution of the ODF over time in Fig. 11, which shows the Bingham representation at different steps for the case of driving stress and  $\zeta_*^\Xi = 10$ .

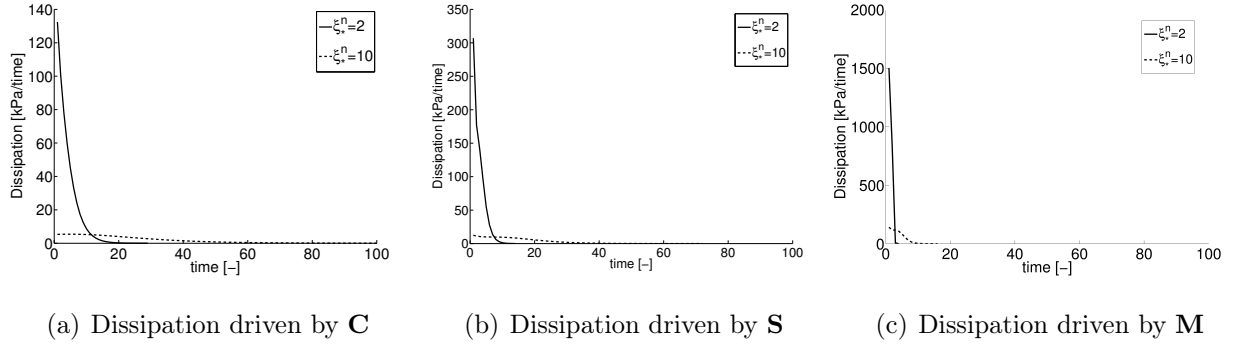


Figure 10: Dissipative evolution  $\mathcal{D}_{rep}$  for the different driving quantities and  $\zeta_*^{\Xi} = 2$  and  $\zeta_*^{\Xi} = 10$ .

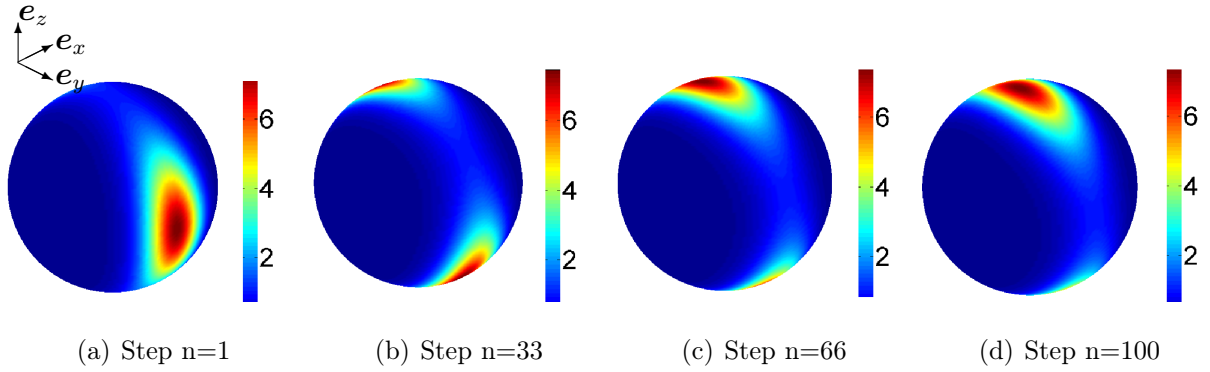


Figure 11: Evolution of the ODF for different steps. (a) the distribution at step 0, (b) for step 33, (c) for step 66 and finally (d) at the end of the analysis.

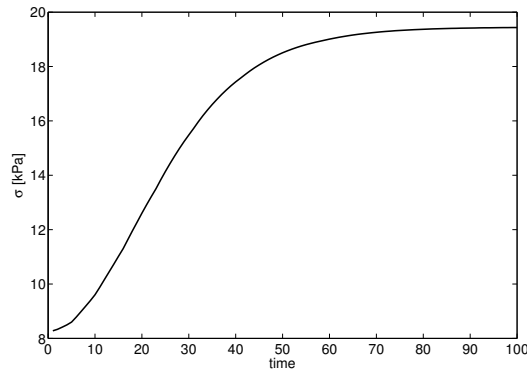


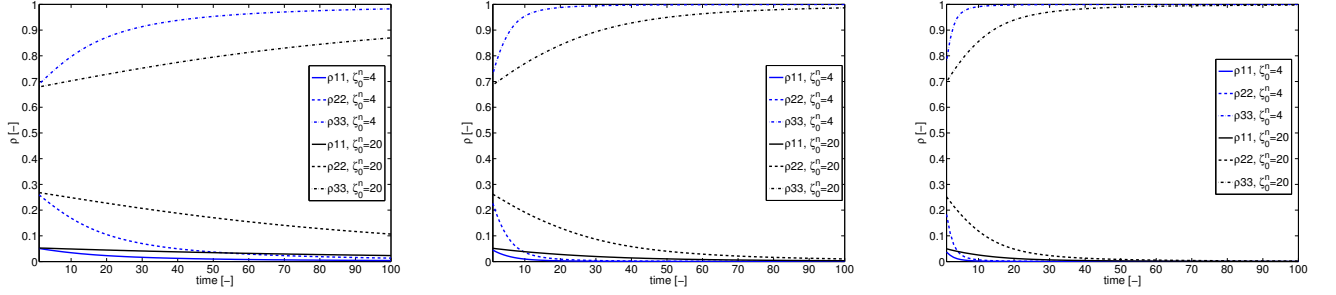
Figure 12: Stress evolution for the reorientation case shown in Fig. 11.

$\zeta_*^{\Xi} = 2$			$\zeta_*^{\Xi} = 10$		
strain	stress	Mandel	strain	stress	Mandel
$5.328 \times 10^2$	$8.269 \times 10^2$	$5.912 \times 10^4$	$1.730 \times 10^2$	$2.239 \times 10^2$	$6.742 \times 10^3$

Table 3: Energy dissipated for each type of driving quantity.

## 6.2. Reorientation of the fibrils

In this section we give some examples to illustrate the model described in Section 3.2, where the fibrils or filaments that make up a fibered structure reorient themselves with the maximum eigenvector of a given driving quantity. The material parameters of the WLC model are fixed for all the examples to the same values given in the above section,  $r_0 = 1$ ,  $L = 2$ ,  $A = 1.3$ ,  $n = 7.0 \times 10^{21}$ ,  $k = 1.381 \times 10^{-23} J/K$  and  $\theta = 300K$ . All specimens are stretched with  $\mathbf{F} = 1/\sqrt{\lambda} \mathbf{e}_x \otimes \mathbf{e}_x + 1/\sqrt{\lambda} \mathbf{e}_y \otimes \mathbf{e}_y + \lambda \mathbf{e}_z \otimes \mathbf{e}_z$  with  $\lambda = 2$  instantaneously applied and maintained to the end of the reorientation. We set  $\Delta t = 0.01$ . The Bingham parameters are  $\kappa_{1,2,3} = [0, 8, 10]$  and  $\mathbf{Q} = \mathbf{I}$  (being  $\mathbf{I}$  being the second order identity tensor). We therefore ensure that the principal direction of the structure is previously aligned with the maximum principal direction of the driving quantity. We introduce the biological perspective by means of the material parameter  $\bar{\zeta}^{\Xi}$  defined in Eq. 26. Moreover, as in the previous section, we have included the material parameter  $\bar{\zeta}_*^{\Xi}$ , which is fixed to  $\bar{\zeta}_*^{\Xi} = 4, 20$  for comparison. This corresponds to a value twice  $\zeta_*^{\Xi}$ . As in the case of the macro remodeling, we carry out the process using the different driving quantities. In Fig. 13, we present the evolution of the diagonal components of  $\boldsymbol{\rho}$  (Eq. 13), which measure the concentration of the fibrils.



(a) Evolution of the microstructure distribution driven by **C** (b) Evolution of the microstructure distribution driven by **S** (c) Evolution of the microstructure distribution driven by **M**

Figure 13: Evolution of the microstructure by means of the diagonal components of  $\rho$ .

Again, the remodeling driven by strain is shown to be the slowest, followed by Mandel and stress. The processes with  $\bar{\zeta}_*^E = 20$  are slower than those with  $\bar{\zeta}_*^E = 4$ , as expected.

We also show (Fig. 14) the evolution of the fibrils as the evolution of the integration directions.

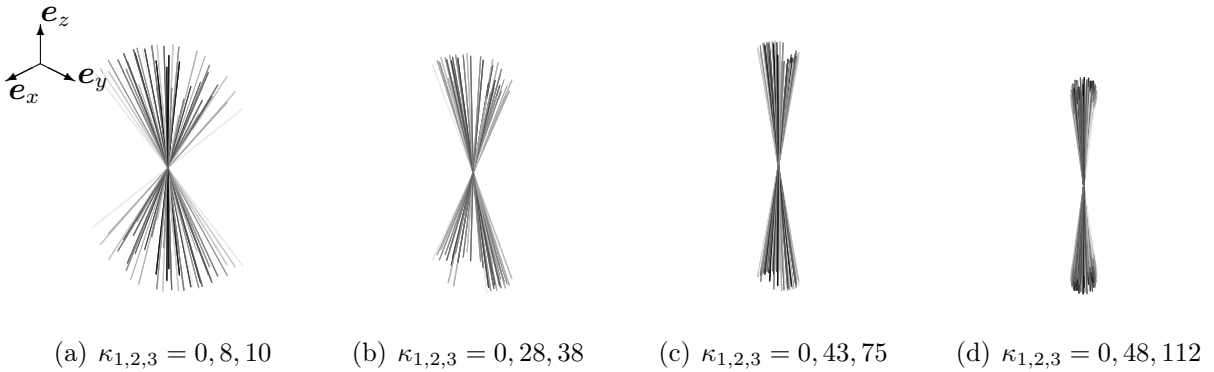


Figure 14: Evolution of the fibrils for different steps. (a) the initial distribution with  $\kappa_{1,2,3} = 0, 8, 10$ , (b) for step 33 leading to  $\kappa_{1,2,3} = 0, 28, 38$ ,  $\kappa_{1,2,3} = 0, 43, 75$  for step 66 in (c) the end of the analysis with  $\kappa_{1,2,3} = 0, 48, 112$  in (d).

In order to view this evolution we make use of the procedure discussed in Remark 1. Fig. 15 shows the Bingham representation at different steps for the case of driving stress and  $\bar{\zeta}_*^E = 20$ . As we can see, its shape tends towards a very concentrated von Mises distribution, i.e., to a 1D single fiber orientation.

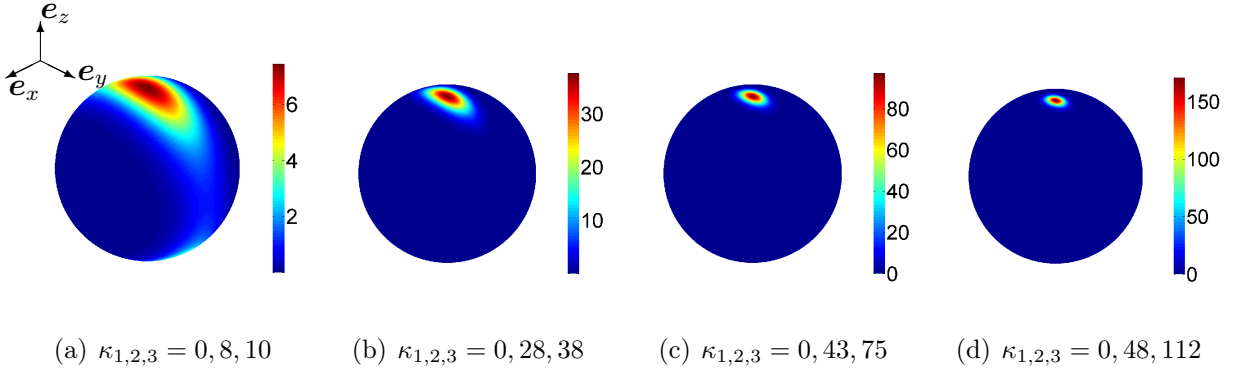


Figure 15: Evolution of the distribution for different steps. (a) the distribution at step 0 with  $\kappa_{1,2,3} = 0, 8, 10$ , (b) for step 33 leading to  $\kappa_{1,2,3} = 0, 28, 38$ ,  $\kappa_{1,2,3} = 0, 43, 75$  for step 66 in Fig. (c), the end of the analysis with  $\kappa_{1,2,3} = 0, 48, 112$  in (d). For  $t \rightarrow \infty$  the Bingham distribution leads to very concentrated von Mises distributions.

To conclude this section, we present the dissipative nature of the model graphically in Fig. 16 and quantitatively in Table 4. The results suggest that the dissipative process is highly sensitive to  $\bar{\zeta}_*^{\Xi}$ . For  $\bar{\zeta}_*^{\Xi} = 4$ , the strain driven problem is the most dissipative, followed by stress and Mandel. However, for  $\bar{\zeta}_*^{\Xi} = 20$ , the strain quantity becomes the least dissipative and the Mandel tensor the most dissipative. Nevertheless, as suggested above, we need experimental data to obtain further conclusions on this issue. In order to compare the dissipative nature of the model presented here with that described in the previous section, we need to compute the dissipation with values of  $\bar{\zeta}_*^{\Xi} = 1$  and  $\zeta_*^{\Xi} = 1$ . In this case the dissipation takes the following values:  $\mathcal{D}_{\mathbf{C}} = 2.636 \times 10^2$  [kPa/time],  $\mathcal{D}_{\mathbf{S}} = 2.636 \times 10^2$  [kPa/time] and  $\mathcal{D}_{\mathbf{M}} = 2.638 \times 10^2$  [kPa/time]. They are almost the same among themselves and very similar to those in the dissipative PDR process. Again, some experimental tests would be helpful in order to reach further conclusions.

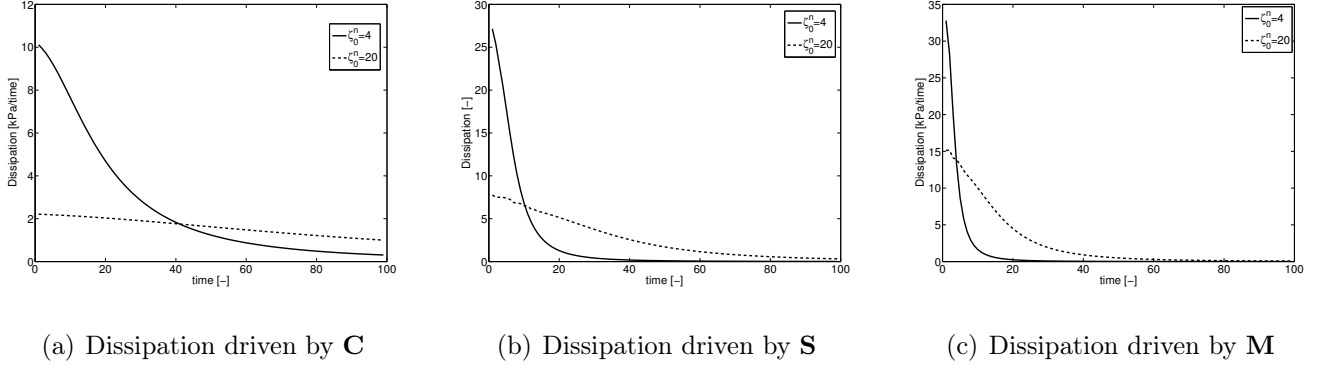


Figure 16: Dissipation of the model for the different driven quantities and material parameters  $\bar{\zeta}_*^{\Xi} = 4, 20$ .

	$\zeta_*^n = 4$			$\zeta_*^n = 20$		
	strain	stress	Mandel	strain	stress	Mandel
$\mathcal{D}$ [kPa/time]	$2.173 \times 10^2$	$2.033 \times 10^2$	$1.690 \times 10^2$	$1.670 \times 10^2$	$2.207 \times 10^2$	$2.199 \times 10^2$

Table 4: Energy dissipated per each type of driving quantity and for  $\bar{\zeta}_*^{\Xi} = 4, 20$ .

**Remark 4.** *Equibiaxial and volumetric states.* Equibiaxial and volumetric loads are special situations that should be carefully treated. We have consider that our model do not evolve under volumetric load. Given that any three orthogonal directions are principal directions of a volumetric state, we can not choose a particular position of the principal directions for **Q** to evolve. In the equibiaxial case, the principal directions will evolve to the plane containing the two maximum stress directions along the direction of minimum length and then they will be equilibrated there due to, again, any direction of that plane is an eigenvector.

**Remark 5.** *No load state.* Another important issue to take into account is the stationarity of the model under no load. As was pointed out by Garikipati et al. (2005), a proposed model must not evolve under an undeformed state. Our model solves this issue by means of the  $\zeta_0^n$  parameter that does not allow any movement in the unloaded state.

## 7. A finite element case: morphological and orientation changes of cells.

In this section we compute a finite element model presenting a biological example of the model discussed above and non-homogeneous states of deformation. We have outlined the main steps of the algorithmic scheme in Table 5. As discussed in the Introduction section, the cells change their mean orientation and morphological shape. The experiments are focused on static loading, where cells align with the direction of stretching, and cyclic mechanical tests, where cells align with the direction of stretching. In the following example we will restrict ourselves to the static loading case. To do so, we model a thin sheet of material, 40mm x 20mm x 0.5 mm, as shown in Fig. 17(a), and discretized in 800 hexahedral elements. This geometry represents a classical case of PDMS sheet used for cell tests. The left side of the specimen is fixed while displacement or force are imposed on the right side. In fact, we investigate the influence of both cases of boundary condition. We first compute the imposed displacement case, with a stretch value of 50% of the initial length in  $\mathbf{e}_x$ . We retrieve the reaction forces, before remodeling, on the right side of the model to be imposed subsequently in a force driven simulation. Obviously, the stress and strain field over the specimen is the same in both cases before remodeling, but their evolution is different for the Neumann and Dirichlet boundary value problems. Moreover, to allow a more general simulation of the distribution of the cells, as is usually the case in experimental procedures, we set a random orientation of the cell in each integration point as well as the concentration values of the statistical distribution  $\kappa_{1,2,3}$ . The random values are obtained by means of the built-in function of a commercial software package (MATLAB 6.1, The MathWorks Inc., Natick, MA, 2000). We also describe the evolution of the micro-structural information. In order to do so, in the following results we look at three different points of the material which are in some way meaningful. They are shown in Fig. 17(a) as points 1, 2 and 3, and will be referred to as such in the following. The values are described in Fig. 17(b-d).

Table 5: Algorithm to compute remodeling of cell-like structures.

---

**Input:**  $\mathbf{F}^{j+1}$ , **internal variables at time  $j$**

---

I Evaluate kinematics  $\mathbf{C}^{j+1}$  and constitutive equations  $\Psi^{j+1}$ ,  $\mathbf{S}^{j+1}$  and  $\mathbf{M}^{j+1}$

II Compute stimulus tensor  $\Xi$  by  $\mathbf{C}^{j+1}$ ,  $\mathbf{S}^{j+1}$  or  $\mathbf{M}^{j+1}$

III Update orientation variables.

Evaluate exponential mapping for the evolution of  $\mathbf{Q}^{j+1}$  and  $\mathbf{r}_i^{j+1}$

$$\mathbf{Q}^{j+1} = \exp(\zeta^{\Xi} \hat{\omega} \Delta t / \zeta_*^{\Xi}) \cdot \mathbf{Q}^j \quad (29)$$

$$\mathbf{r}_i^{j+1} = \exp(\bar{\zeta}^{\Xi} \hat{\omega}_i \Delta t / \bar{\zeta}_*^{\Xi}) \cdot \mathbf{r}_i^j \quad (30)$$

IV Update statistical distribution  $\rho_i^{j+1}(\mathbf{r}^{j+1}; \mathbf{Q}, \mathbf{Q}^{j+1})$  based on Eq. 6 and spatial description of the orientation vector of the fibrils as  $\bar{\mathbf{t}}_i^{j+1} = \mathbf{F}^{j+1} \cdot \mathbf{r}_i^{j+1}$ . These updates make the constitutive model to evolve. .

V Compute dissipation,  $\mathcal{D}_{\text{PDR}}$  and  $\mathcal{D}_{\text{RF}}$  as described in Eq. 21 and Eq. 22 and anisotropy  $\delta$  as in Eq. 28.

VI Calculate stresses  $\boldsymbol{\tau}^{j+1}$  and tangent operator related to the Jaumann rate as

$$\boldsymbol{\tau}^{j+1} \approx 2\mathbf{b}^{j+1} \cdot (C_1 - C_2 I_1^{j+1}) + \sum_{i=1}^m \rho_i^{j+1} \boldsymbol{\tau}_i^{j+1} w_i \approx \sum_{i=1}^m [\rho_i^{j+1} \psi'(\bar{\lambda}_i) \bar{\lambda}_i^{-1} \bar{\mathbf{t}}_i^{j+1} \otimes \bar{\mathbf{t}}_i^{j+1}] w_i$$

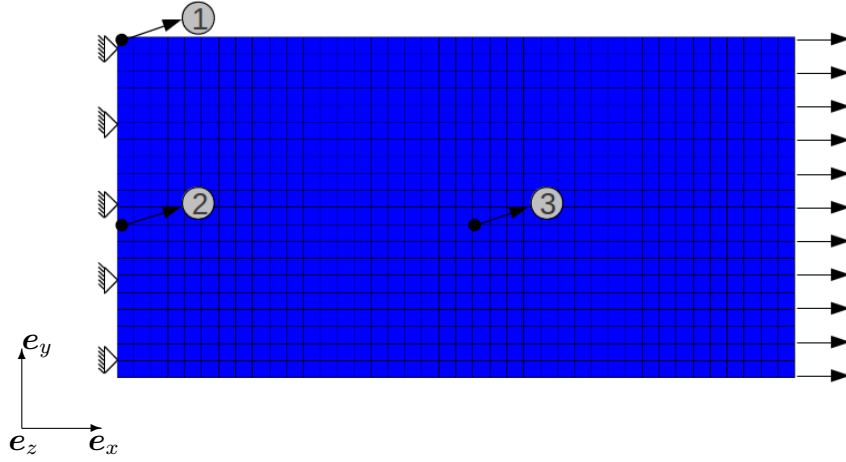
$$\overset{\nabla}{\mathbf{c}}^{j+1} = [\mathbf{c}^{j+1} + 1/2[\delta \tau^{j+1} + \tau^{j+1} \delta + \delta \tau^{j+1} + \tau^{j+1} \delta]]/J \quad \text{with}$$

$$\mathbf{c}^{j+1} \approx \sum_{i=1}^m n \rho_i^{j+1} w_i [\psi_i''^{j+1} - \psi_i'^{j+1} \bar{\lambda}^{-1}] \bar{\lambda}^{-2} \bar{\mathbf{t}}_i^{j+1} \otimes \bar{\mathbf{t}}_i^{j+1} \otimes \bar{\mathbf{t}}_i^{j+1} \otimes \bar{\mathbf{t}}_i^{j+1}$$

---

**Output:**  $\boldsymbol{\tau}^{j+1}$ ,  $\overset{\nabla}{\mathbf{c}}^{j+1}$ ,  $\mathbf{Q}^{j+1}$ ,  $\mathbf{r}^{j+1}$ ,  $\mathcal{D}_{\text{PDR}}$ ,  $\mathcal{D}_{\text{RF}}$ ,  $\delta$

---



(a) Geometry and boundary conditions of the finite element model. Point 1, 2 and 3 have been marked for micro-structural plotting purposes.

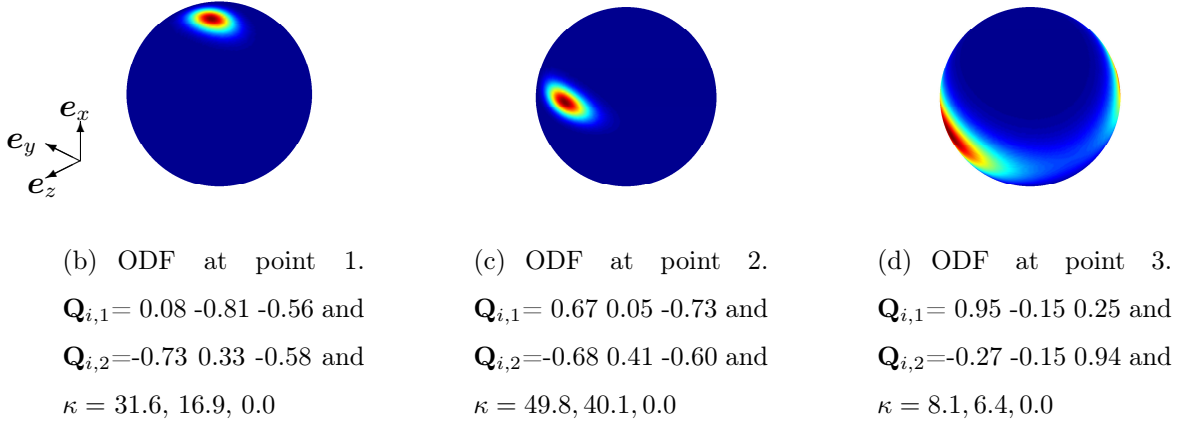


Figure 17: Description of the boundary condition (a), initial values of the ODF distribution for the three marked points (b-d).

The stress field in the deformed configuration is shown in Fig. 18. For the sake of simplicity we will compute strain and stress-driven problems, since they are the most commonly used variables and can be easily compared with those given in the literature. Moreover, and again to keep the problem as simple as possible, we set  $\zeta_*^{\Xi}, \zeta_*^{\Xi}, \bar{\zeta}_*^{\Xi}$  and  $\bar{\zeta}_*^{\Xi}$  equal to one, and as we demonstrated in Section 6, trends and values of remodeling in Mandel-driven cases remain between those achieved by strain- and stress-driven problems. In Fig. 19 we plot the reaction force and the displacement on the right side of the phantom for the displacement

and force driven problem respectively. We can see how the reaction force increase due to the reorientation of the micro-structure in the Dirichlet boundary condition problem and how the sample in the Neumann boundary condition case shorten. We also present stress and anisotropy fields for every boundary problem discussed above for different time steps in Figs. 20,21, 22 and 23. Fig 20(a-b) show the evolution of the anisotropy for the strain driven problem in the Dirichlet boundary problem and the Neumann boundary problem (c-d), respectively. The evolution of both problems shows an anisotropic measure value close to zero, but a different final geometry. The Neumann case undergoes a clear shortening due to the alignment of the cells in the direction of the stretching. This behavior is obviously observed in all the following cases. The anisotropic evolution for the stress driven problem also leads to a very low value of the anisotropic measure, although some points show higher values of anisotropy. This is due to the more unstable nature of the evolution of the eigenvectors of the stress tensor while in the strain driven problem the principal directions maintains an almost constant direction. The stress increases in the Dirichlet case since the structure reorients in the direction of the load and the fixed imposed displacement. The Neumann boundary cases (22(c-d),23(c-d)), although the reorientation also occurs also in the direction of the load, show a decrease in the stresses due to the stiffening of the material and the fixed applied force. In the Dirichlet boundary problem (22(a-b),23(a-b)) the stresses notably increase because of the alignment of the structural element in the direction of the stretching, which maintain a constant value.

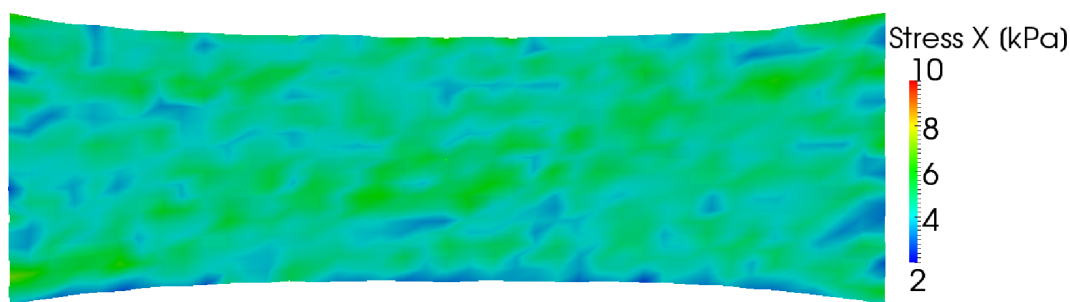
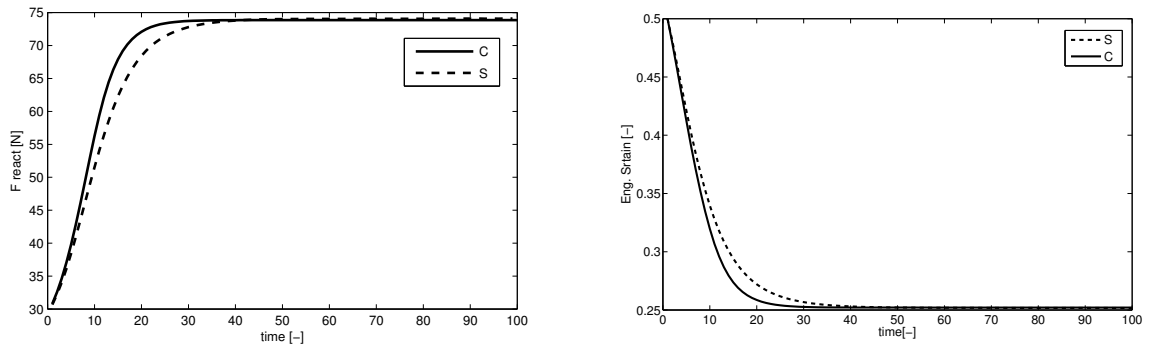
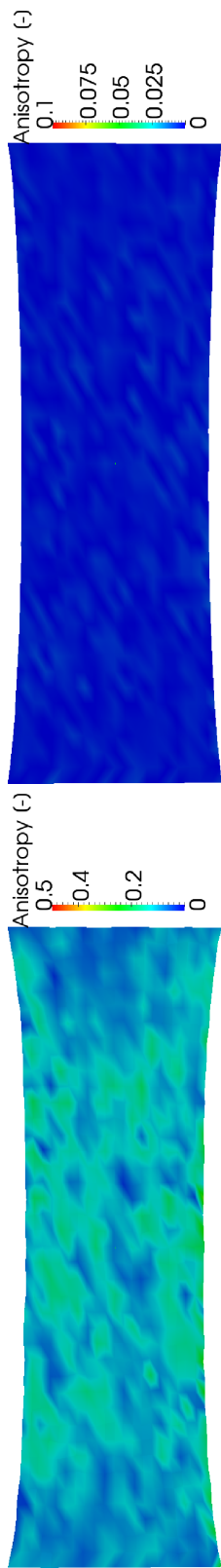


Figure 18: Maximal principal stress for the static simulation. The stress field shows a highly non-uniform distribution of stresses due to the random distribution of the micro-structure.

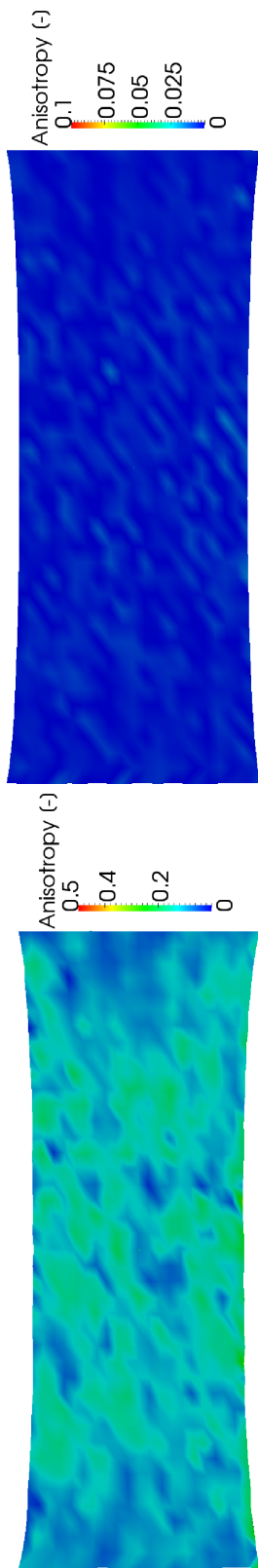


(a) Evolution of the reaction forces for the displacement driven problem. Dirichlet boundary problem. (b) Evolution of the engineering deformation for the force driven problem. Neumann boundary problem.

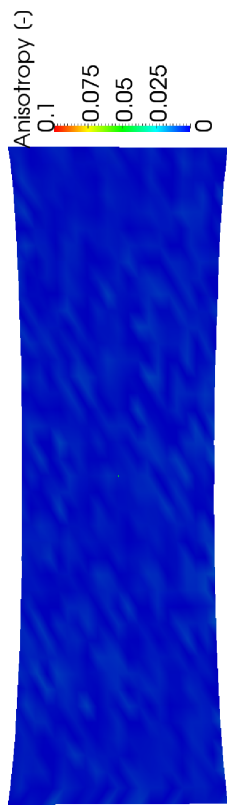
Figure 19: Evolution of the displacement and reaction forces for different boundary conditions problems.



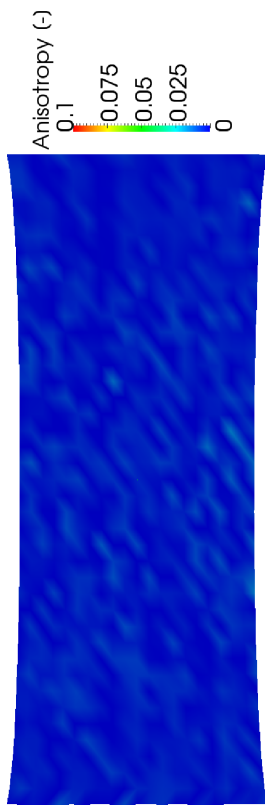
(a) Anisotropy field at time step 10.



(c) Anisotropy field at time step 10.

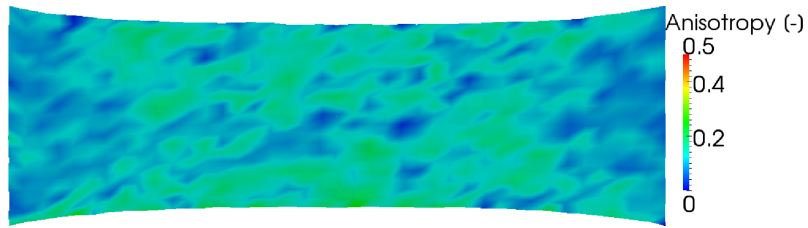


(b) Anisotropy field at time step 100.

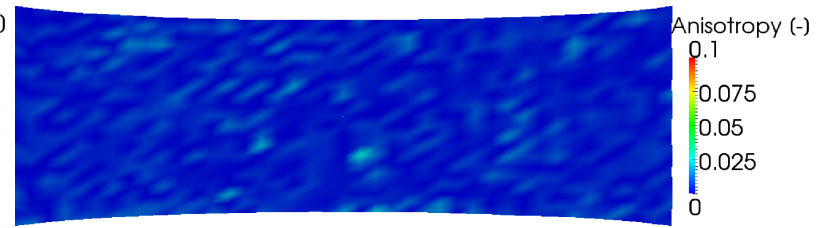


(d) Anisotropy field at time step 100.

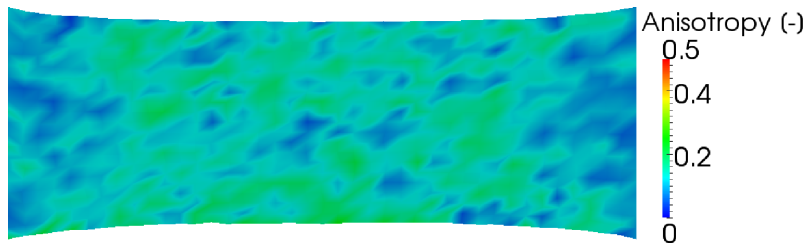
Figure 20: Evolution of anisotropy for different boundary value problems, Dirichlet (a-b) and Neumann (c-d) for remodeling driven by strain.



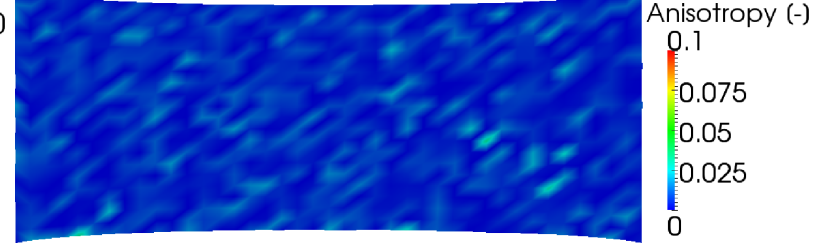
(a) Anisotropy field at time step 10.



(b) Anisotropy field at time step 100.

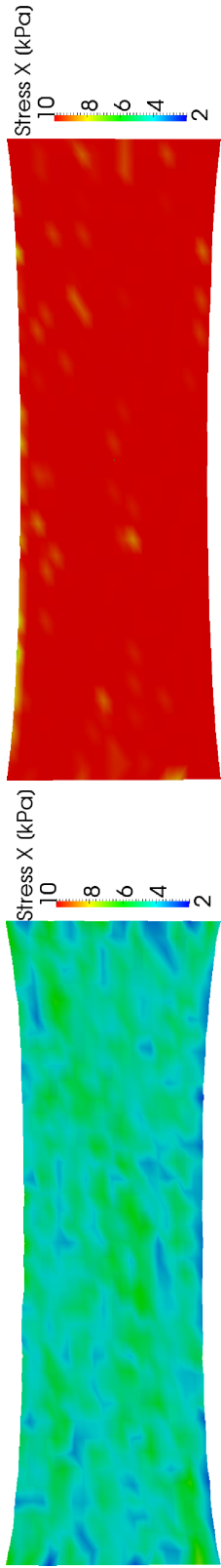


(c) Anisotropy field at time step 10.

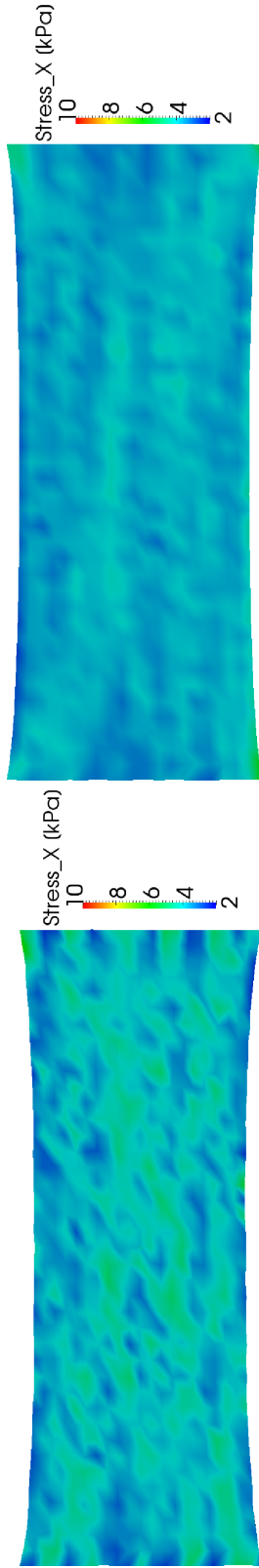


(d) Anisotropy field at time step 100.

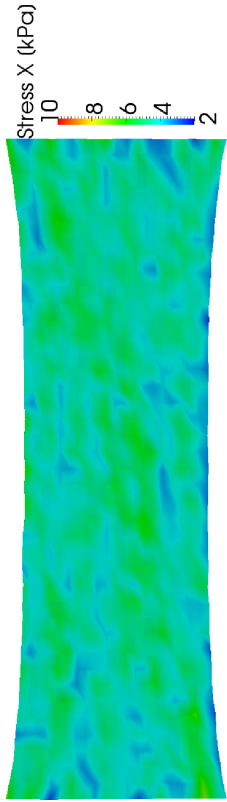
Figure 21: Evolution of anisotropy for different boundary value problems, Dirichlet (a-b) and Neumann (c-d) for remodeling driven by stress.



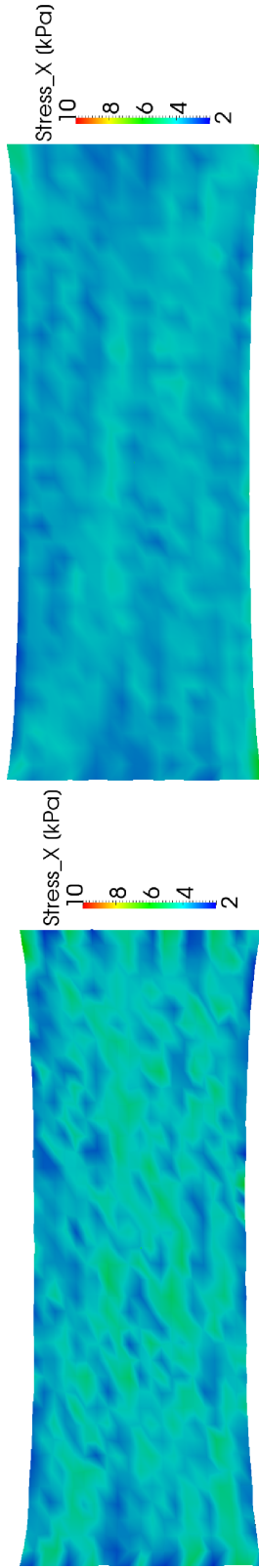
(a) Cauchy stress components  $\sigma_x$  at time step 10.



(b) Cauchy stress components  $\sigma_x$  at time step 100.



(c) Cauchy stress components  $\sigma_x$  at time step 10.

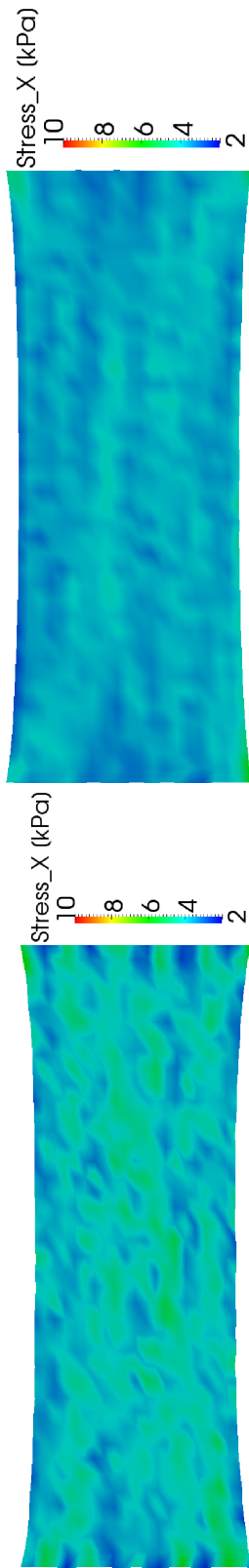


(d) Cauchy stress components  $\sigma_x$  at time step 100.

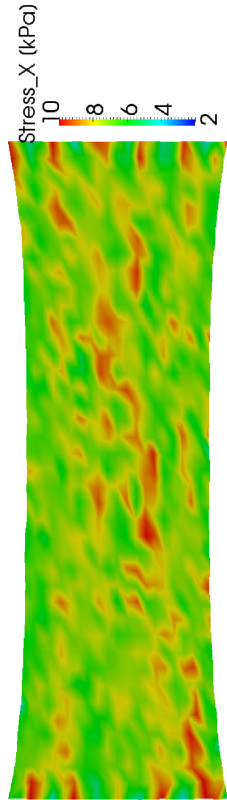
Figure 22: Evolution of stress for different boundary value problems, Dirichlet (a-b) and Neumann (c-d) for remodeling driven by strain.



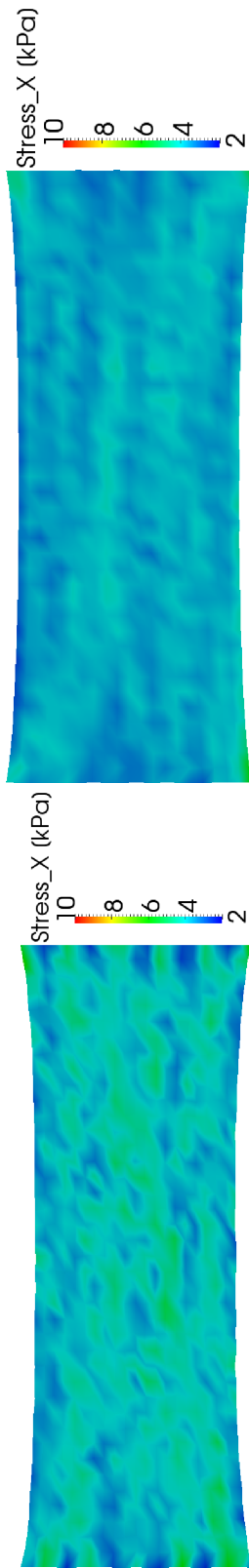
(a) Cauchy stress components  $\sigma_x$  at time step 10.



(b) Cauchy stress components  $\sigma_x$  at time step 100.



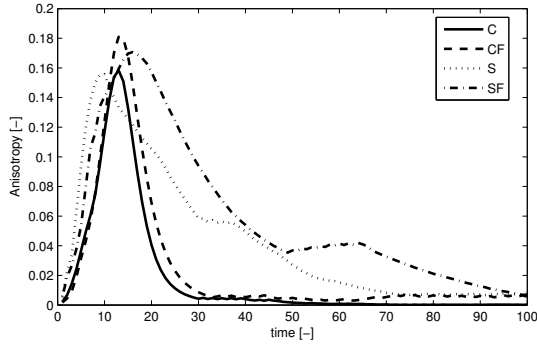
(c) Cauchy stress components  $\sigma_x$  at time step 10.



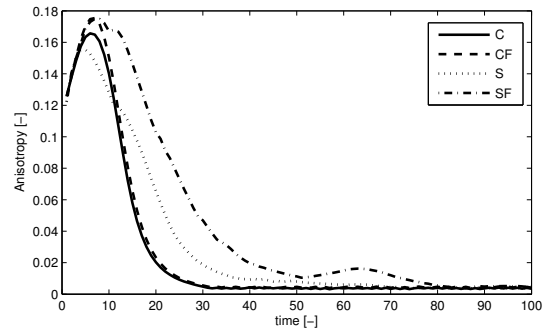
(d) Cauchy stress components  $\sigma_x$  at time step 100.

Figure 23: Evolution of stress for different boundary value problems, Dirichlet (a-b) and Neumann (c-d) for remodeling driven by stress.

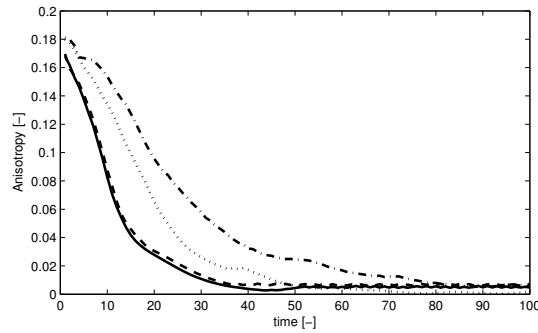
We now look at the evolution of the micro-structure. First, we present the anisotropy evolution in Fig. 24. The figures show a less uniform evolution than that of the cases presented in Section 6 due to the non-uniform deformation state. All three points end up with an anisotropy measure close to zero, which represents a bundle aligned with the direction of maximum strain. Due to the random orientation and concentration of the cells of interest, the initial anisotropy value is also different for the three of them. The stress driven cases show a less uniform evolution of the anisotropy due to the non-regular evolution of the stresses. The evolution for the two cases of strain driven problems show very similar features while stress driven problems present a different behavior, occurring at a lower rate in the Neumann boundary case. In the strain-driven case, anisotropy evolution is very similar since eigenvectors of the strain tensor are almost constant. In the Dirichlet case,  $\xi^\Xi$  also maintain a constant value while in the Neumann case, this parameter decrease since the sheet shorten. In the stress-driven problem, the Neumann case have a noticeable slower evolution rate. This is because the stresses decrease during the shortening process and the parameter  $\xi^\Xi$  become considerable smaller which makes the evolution rate to decrease. Moreover, the stress evolution of each individual structure is influenced by the current stress state of the surrounding structures.



(a) Evolution for Point 1.



(b) Evolution for Point 2.



(c) Evolution for Point 3.

Figure 24: Anisotropy evolution for the three points of interest for strain (C and CF) and stress (S and SF) driven problems and different boundary conditions, Dirichlet (C and S) and Neumann (CF and SF).

## 8. Discussion

The adaptation of biological tissues has been a very active research field in recent years. The three principal processes of adaptation of biological tissue to mechano-chemical stimuli from a continuum point of view are remodeling, growth and morphogenesis (see e.g. Humphrey (2009); Taber (2009); Ambrosi et al. (2011)). In this contribution we have focused on the reorientation process of fibered biological structures, proposing a complete 3D model that accounts for the reorientation of both the main direction of the structure and the fibrils or filaments that compose such a fibered structure. Most previous works have described the reorientation of a simple 1D fiber while, more recently, some others have taken into account the remodeling of the underlying structure by means of changes in its statistical

distribution (Baaijens et al., 2010; Menzel et al., 2008).

Our approach extends the models mentioned above in order to develop a new model capable of describing both the remodeling of the principal direction and the distribution of the micro-structure at the same time, allowing a multi-scale description of the remodeling in biological fibered structures. Moreover, we study the dissipation process from a mechanical point of view and describe the process based on different mechanical variables. These latter factors are not usually dealt with in similar studies. We have considered a microsphere-based model that has allowed us to include the two aspects of the problem. A multi-scale scheme that couples the microstructural behavior and the macroscopic scale is used, also allowing the fibered microstructure to be defined in terms of the fibrils or filaments that make it up. We also extend the usual orientation space description of the micro-sphere model so that it is associated to a physical space, or a 3D representation of the fibered structure.. In this way, we compute the reorientation of the mean direction at the macro-scale and the reorientation of the microstructure, upscaling the variables in the lower scale to the macroscopic behavior by means of a homogenization scheme.

Numerous works have analyzed different types of driving quantities in these processes (see e.g. Kuhl et al. (2005); De et al. (2008); Baaijens et al. (2010) and references therein), stress and strain being the most common. We have considered three driving quantities, strain, stress and a mix-variant Mandel-type tensor, for driving the reorientation process. We assume the principal directions of these quantities as the stimulus to drive the reorientation process. To complete the model, we have included two further material parameters. The first takes into account the magnitude of the driving quantities, since it seems natural to assume that the magnitude influences the evolution rate. The second parameter has been included to reflect the fact that different living structures can react to the same load in different ways.

Our results showed material-dependent results in terms of the energy dissipated during the process. Dissipation due to remodeling is not an easy variable to measure and to best of our knowledge this has been never achieved. It is a much easier task to fit the material parameters by means of the remodeling evolution than by dissipative aspects. Dissipation

is a chemical-dependent process, particularly in biological issues. We did not take this into account in our model, mainly because the number of parameters and coupled processes involved would have made the problem unmanageable. Looking at the mechanical results without taking into account material parameters (see Section 3), strain appears as the most dissipative quantity and stress the least dissipative. Once biological parameters are introduced, as in Section 6, the results become inconclusive. At this point, we can affirm that a mechanical description alone does not provide a sufficient indication about dissipation in biological matter. To obtain more accurate results, the chemical part of the process needs to be examined in order to throw light on the mechanical effects of the process. Furthermore, the model should be adapted to the specific problem at hand.

In terms of remodeling and structural organization, the results were clearer. Given the nature of our model, higher values of  $\zeta_*^E$  produce higher rates of remodeling. This material parameter would be easier to fit if very accurate results were required. Moreover, given the nonlinearity of stresses and strains, the coefficient considered in Eqs. 24 and 26 can become disproportionate and can outweigh the effect of the stimuli. This is specially true of the Mandel problem. Note also that these parameters are quite difficult to fit and a complete set of experimental tests should be done at different strain and stress levels (and therefore with different degrees of matrix stiffness) while measuring the evolution of the structure.

There have been important discussions about what stimuli control cell remodeling. In many of these works (see e.g. Saez et al. (2005); Discher et al. (2005)) focus on the force that cells exert in different matrices. However, our approach looks at the behavior of cells when they are mechanically stimulated. Our model predicts, under the stress driven problem, that cells remodel themselves. In a displacement control test with a very stiff matrix is considered, for example in the case of a polycarbonate-like material, the stress values in the material would be higher than those achieved in a softer matrix for the same displacement. This stiffer material would produce a much higher rate of remodeling, which from our understanding is something that does not in fact occur. Our view is that strain is more likely to drive this kind of process. Strain over the matrix does actually boost strain over the cell and therefore stress. Whether strain or stress within the cell is the real stimulus is a question

that cannot be answered within the confines of this work. Strains of integrin adhesions and the glycocalyx due to matrix deformation might be likely candidates for triggering the remodeling machinery. However, we want to point out that the present model establish a general framework for studying remodeling of biological structures at different scales. To be able to obtain accurate and conclusive results in the field of cell mechanics research is needed by means of specific experiments and evolution equations.

After having presented some analytical cases of our model in order to study its behavior under different material parameters, we included it in a finite element scheme. This allowed us to compute a more realistic biological problem and non-uniform deformation states in problems with different boundary conditions. We studied the remodeling of a plaque made up of a matrix seeded by a cell colony. The initial orientation values and shape were assumed to be random and our simulation showed a good qualitative agreement with the experimental findings. They showed progressive orientation of the principal orientation and a change in the initial shape due to the reorganization of the interior structure. The results of the reorganization fit qualitatively well with experimental results given in the literature. For example, Farcas et al. (2009) presented results (Fig. 25) for endothelial cells under shear stress that after 24 hours showed both an alignment of the cells and a narrowing of their shape. Our simulations are consistent with these findings.

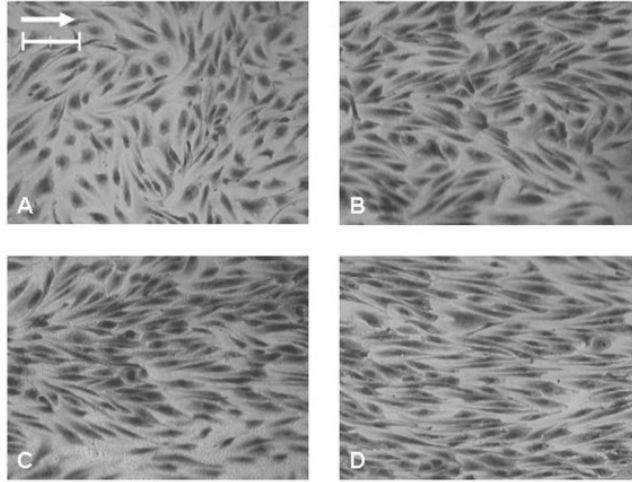


Figure 25: Results presented by (Farcas et al., 2009) (with permission) in a shear stress experiment. From a random distribution and shape of the cells, they obtain a more narrow shape and an alignment of their principal directions along the flow direction. The same feature is observed in the simulations reported in Section 6.

The presented model has a strong capability for characterizing the evolution of complex biological fibered structures such as, for example, collagen bundles or cells. However, there are certain limitations which need to be overcome to significantly improve it. The first, which does not apply only to our model, is the determination of the parameters related with the reorientation rate. For example, in a cell stretched by its substrate, the tracking of microtubules could help to fit not the material parameters and the driving quantities that better fit the experiments could be identified. It is important to note that this cellular process is highly dependent on other non-mechanical triggers for adaptation, such as chemical interactions. Such stimuli boost many other transduction phenomena that ultimately lead to structural adaptation, substance synthesis and genetic expression. These aspects should to some extent be considered in our model to make it more accurate and realistic.

The use of a Bingham distribution to reflect the fiber or cell distribution is simple but also has some drawbacks. Although useful for a first attempt, is possible not the best option if an real cell structure want to be analyzed. The tracking of microtubules and stress fiber mentioned above could be used to reconstruct a more realistic cell structure within the

micro-sphere-based approach, which can be used to compute both the reorientation of the fibrils and the homogenized variables, e.g. stresses. Currently, we have a fixed position over the unit sphere, and the number of directions contributing to the mechanical behavior is limited by the shape of the statistical function. Related to this latter issue, another limitation derives from the integration scheme in an anisotropic framework. Alastrué et al. (2009b) presented a non linear transformation of the integration directions, in accordance with the von Mises statistical distribution used.

From our point of view, the most important future work would be to focus on extending the model to the numerical simulation of cell mechanics. However, the amount of information needed is huge. For example, the active force exerted by the stress fibers due to external stimuli, the amount of actin generated by a mechanical stimulus, the dynamics of polymerization of actin and tubulin, the evolution of endothelial cells due to changes in the wall shear stress in blood vessels, and much more. Although the experiments needed to accurately fit such theoretical and computational models are very sophisticated and require expensive instruments, the models can at least provide interesting mathematical descriptions of these important biological processes.

In short, we have proposed a novel general 3D reorientation model for both the principal direction of the whole structure and the underlying fibered structure. Our aim in this work is to establish a mechanical framework for the structural remodeling of hierarchical arrangements and evaluate variables such as the evolution of the anisotropy, dissipation or stresses. This approach allows the modeling of different remodeling processes in biological tissue, and with the appropriate experiments could lead to a better knowledge of how biological tissue adapts to its specific environment. For example, combined with the development of a growth model (see Humphrey (2009); Ambrosi et al. (2011)), our approach could help to model and predict the overall behavior of arterial tissue reacting to external stimuli by means of remodeling the microstructure and growth (positive or negative) of its constituents.

## 9. Acknowledgements

Support from the Spanish Ministry of Research and Innovation through the research projects DPI2010-20746-C03-01 and through the grant BES-2009-028593, as well as support from the CIBER initiative, is highly appreciated. CIBER-BBN is an initiative funded by the VI National R&D&I plan 2008-2011, Iniciativa Ingenio 2010, Consolider Program, CIBER Actions and financed by the Instituto de Salud Carlos III with assistance from the European Regional Development Fund. We would also like to thank Dr. Jose Felix Rodriguez for his help and wise advice.

- Alastrué, V., Saez, P., Martinez, M. A., Doblare, M., Dec. 2010. On the use of the bingham statistical distribution in microsphere-based constitutive models for arterial tissue. *Mech Res Commun* 37 (8), 700–706.
- Alastrué, V., Martinez, M. A., Doblare, M., Menzel, A., Jan. 2009a. Anisotropic micro-sphere-based finite elasticity applied to blood vessel modelling. *J Mech Phys Solids* 57 (1), 178–203.
- Alastrué, V., Martinez, M. A., Menzel, A., Doblare, M., Jul. 2009b. On the use of non-linear transformations for the evaluation of anisotropic rotationally symmetric directional integrals. application to the stress analysis in fibred soft tissues. *Intl J Numer Meth Eng* 79 (4), 474–504.
- Alford, P., Humphrey, J., Taber, L., 2008. Growth and remodeling in a thick-walled artery model: effects of spatial variations in wall constituents. *Biomech Model Mechan* 7, 245–262.
- Ambrosi, D., Ateshian, G. A., Arruda, E. M., Cowin, S. C., Dumais, J., Goriely, A., Holzapfel, G. A., Humphrey, J. D., Kemkemer, R., Kuhl, E., Olberding, J. E., Taber, L. A., Garikipati, K., Apr. 2011. Perspectives on biological growth and remodeling. *J Mech Phys Solids* 59 (4), 863–883.
- Arruda, E. M., Boyce, M. C., Feb. 1993. A three-dimensional constitutive model for the large stretch behavior of rubber elastic materials. *J Mech Phys Solids* 41 (2), 389–412.
- Ateshian, G. A., Nov. 2007. On the theory of reactive mixtures for modeling biological growth. *Biomech Model Mechan* 6 (6), 423–445.
- Baaijens, F., Bouten, C., Driessen, N., Jan. 2010. Modeling collagen remodeling. *J Biomech* 43 (1), 166–175.
- Bazant, P., Oh, B. H., 1986. Efficient numerical integration on the surface of a sphere. *ZAMM-Z Angew Math Comput Me* 66 (1), 37–49.
- Bazant, Z. P., Oh, B. H., 1985. Microplane model for progressive fracture of concrete and rock. *J Eng Mech-ASCE* 111 (4), 559–582.
- Bazant, Z. P., Prat, P. C., Oct. 1988. Microplane model for brittle-plastic material .i. theory. *J Eng Mech-ASCE* 114 (10), 1672–1687.

- Ben Amar, M., Goriely, A., Oct. 2005. Growth and instability in elastic tissues. *Journal of the Mechanics and Physics of Solids* 53 (10), 2284–2319.
- Bingham, C., 1974. An antipodally symmetric distribution on the sphere. *Ann Stat* 2 (6), 1201–1225.
- Bischoff, J. E., Arruda, E. A., Grosh, K., Sep. 2002. A microstructurally based orthotropic hyperelastic constitutive law. *J Appl Mech* 69 (5), 570–579.
- Bischofs, I. B., Schwarz, U. S., Aug. 2003. Cell organization in soft media due to active mechanosensing. *Proceedings of the National Academy of Sciences of the United States of America* 100 (16), 9274–9279.
- Bustamante, C., Bryant, Z., Smith, S. B., Jan. 2003. Ten years of tension: single-molecule DNA mechanics. *Nature* 421 (6921), 423–427.
- Caner, F. C., Carol, I., Jun. 2006. Microplane constitutive model and computational framework for blood vessel tissue. *J Biomech Eng* 128 (3), 419–427.
- Carol, I., Jirasek, M., Bazant, Z., Apr. 2001. A thermodynamically consistent approach to microplane theory. part i. free energy and consistent microplane stresses. *Int J Solids Struct* 38 (17), 2921–2931.
- Carol, I., Jirasek, M., Bazant, Z. P., Jan. 2004. A framework for microplane models at large strain, with application to hyperelasticity. *Int J Solids Struct* 41 (2), 511–557.
- Chen, B., Kemkemer, R., Deibler, M., Spatz, J., Gao, H. J., Nov. 2012. Cyclic stretch induces cell reorientation on substrates by destabilizing catch bonds in focal adhesions. *Plos One* 7 (11), e48346.
- Collinsworth, A. M., Torgan, C. E., Nagda, S. N., Rajalingam, R. J., Kraus, W. E., Truskey, G. A., Nov. 2000. Orientation and length of mammalian skeletal myocytes in response to a unidirectional stretch. *Cell and Tissue Research* 302 (2), 243–251.
- Cowin, S. C., Jan. 1994. Optimization of the strain-energy density in linear anisotropic elasticity. *J Elasticity* 34 (1), 45–68.
- Cowin, S. C., 2004. Tissue growth and remodeling. *Annu Rev Biomed Eng* 6, 77–107.
- Dai, G. H., Kaazempur-Mofrad, M. R., Natarajan, S., Zhang, Y. Z., Vaughn, S., Blackman, B. R., Kamm, R. D., Garcia-Cardena, G., Gimbrone, M. A., Oct. 2004. Distinct endothelial phenotypes evoked by arterial waveforms derived from atherosclerosis-susceptible and -resistant regions of human vasculature. *Proceedings of the National Academy of Sciences of the United States of America* 101 (41), 14871–14876.
- De, R., Safran, S. A., Sep. 2008. Dynamical theory of active cellular response to external stress. *Physical Review E* 78 (3), 031923.
- De, R., Zemel, A., Safran, S. A., Sep. 2007. Dynamics of cell orientation. *Nat Phys* 3 (9), 655–659.
- De, R., Zemel, A., Safran, S. A., Mar. 2008. Do cells sense stress or strain? measurement of cellular orientation can provide a clue. *Biophys J* 94 (5), L29–L31.
- Discher, D. E., Janmey, P., Wang, Y. L., Nov. 2005. Tissue cells feel and respond to the stiffness of their substrate. *Science* 310 (5751), 1139–1143.

- Driessen, N. J. B., Cox, M. A. J., Bouten, C. V. C., Baaijens, F. P. T., Apr. 2008. Remodelling of the angular collagen fiber distribution in cardiovascular tissues. *Biomech Model Mechan* 7 (2), 93–103.
- Driessen, N. J. B., Wilson, W., Bouten, C. V. C., Baaijens, F. P. T., Jan. 2004. A computational model for collagen fibre remodelling in the arterial wall. *J Theor Biol* 226 (1), 53–64.
- Farcas, M. A., Rouleau, L., Fraser, R., Leask, R. L., Oct. 2009. The development of 3-d, in vitro, endothelial culture models for the study of coronary artery disease. *Biomedical Engineering Online* 8, 30.
- Faust, U., Hampe, N., Rubner, W., Kirchgessner, N., Safran, S., Hoffmann, B., Merkel, R., Dec. 2011. Cyclic stress at mhz frequencies aligns fibroblasts in direction of zero strain. *Plos One* 6 (12), e28963.
- Flory, P. J., 1961. Thermodynamic relations for high elastic materials. *T Faraday Soc* 57, 829–838.
- Fung, Y. C., 1990. *Biomechanics: Mechanical Properties of Living Tissues*. Springer.
- Galbraith, C. G., Skalak, R., Chien, S., 1998. Shear stress induces spatial reorganization of the endothelial cell cytoskeleton. *Cell Motility and the Cytoskeleton* 40 (4), 317–330.
- Ganghoffer, J. F., Sep. 2010a. Mechanical modeling of growth considering domain variation. part ii: Volumetric and surface growth involving eshelby tensors. *J Mech Phys Solids* 58 (9), 1434–1459.
- Ganghoffer, J. F., Dec. 2010b. On eshelby tensors in the context of the thermodynamics of open systems: Application to volumetric growth. *International Journal of Engineering Science* 48 (12), 2081–2098.
- Ganghoffer, J. F., Haussy, B., Jul. 2005. Mechanical modeling of growth considering domain variation. part 1: constitutive framework. *International Journal of Solids and Structures* 42 (15), 4311–4337.
- Garikipati, K., Arruda, E. M., Grosh, K., Narayanan, H., Calve, S., Jul. 2004. A continuum treatment of growth in biological tissue: the coupling of mass transport and mechanics. *J Mech Phys Solids* 52 (7), 1595–1625.
- Garikipati, K., Narayanan, H., Arruda, E. M., Grosh, K., Calve, S., 2005. Material forces in the context of biotissue remodelling. In: Steinmann, P., Maugin, G. A. (Eds.), *Mechanics of Material Forces*. Springer, New York.
- Garikipati, K., Olberding, J., Narayanan, H., Arruda, E., Grosh, K., Calve, S., Jul. 2006. Biological remodelling: Stationary energy, configurational change, internal variables and dissipation. *J Mech Phys Solids* 54 (7), 1493–1515.
- Gasser, T. C., Ogden, R. W., Holzapfel, G. A., 2006. Hyperelastic modelling of arterial layers with distributed collagen fibre orientations. *J Roy Soc Interface* 3, 15–35.
- Gleason, R. L., Humphrey, J. D., 2004. A mixture model of arterial growth and remodeling in hypertension: Altered muscle tone and tissue turnover. *J Vasc Res* 41 (4), 352–363.
- Goktepe, S., Abilez, O. J., Parker, K. K., Kuhl, E., Aug. 2010. A multiscale model for eccentric and concentric cardiac growth through sarcomerogenesis. *J Theor Biol* 265 (3), 433–42.
- Goli-Malekabadi, Z., Tafazzoli-Shadpour, M., Rabbani, M., Janmaleki, M., Oct. 2011. Effect of uniaxial

- stretch on morphology and cytoskeleton of human mesenchymal stem cells: static vs. dynamic loading. *Biomedizinische Technik* 56 (5), 259–265.
- Goriely, A., Ben Amar, M., Sep. 2007. On the definition and modeling of incremental, cumulative, and continuous growth laws in morphoelasticity. *Biomechanics and Modeling In Mechanobiology* 6 (5), 289–296.
- Grytz, R., Meschke, G., Apr. 2010. A computational remodeling approach to predict the physiological architecture of the collagen fibril network in corneo-scleral shells. *Biomech Model Mechan* 9 (2), 225–235.
- Hayakawa, K., Sato, N., Obinata, T., Aug. 2001. Dynamic reorientation of cultured cells and stress fibers under mechanical stress from periodic stretching. *Experimental Cell Research* 268 (1), 104–114.
- Heo, S., Xu, Y., 2001. Constructing fully symmetric cubature formulae for the sphere. *Math Comput* 70, 269–279.
- Himpel, G., Menzel, A., Kuhl, E., Steinmann, P., Mar. 2008. Time-dependent fibre reorientation of transversely isotropic continua . finite element formulation and consistent linearization. *Intl J Numer Meth Eng* 73 (10), 1413–1433.
- Holzapfel, G. A., Gasser, T. C., Ogden, R. W., Jul. 2000. A new constitutive framework for arterial wall mechanics and a comparative study of material models. *J Elasticity* 61 (1), 1–48.
- Hsu, H. J., Lee, C. F., Kaunas, R., Mar. 2009. A dynamic stochastic model of frequency-dependent stress fiber alignment induced by cyclic stretch. *Plos One* 4 (3), e4853.
- Humphrey, J. D., Dec. 2001. Stress, strain, and mechanotransduction in cells. *J Biomech Eng* 123 (6), 638–641.
- Humphrey, J. D., 2009. Need for a continuum biochemomechanical theory of soft tissue and cellular growth and remodeling. In: *Biomechanical Modelling at the Molecular, Cellular and Tissue Levels*. Springer Vienna.
- Humphrey, J. D., Rajagopal, K. R., Mar. 2002. A constrained mixture model for growth and remodeling of soft tissues. *Math Models Methods Appl Sci* 12 (3), 407–430.
- Imatani, S., Maugin, G. A., 2002. A constitutive model for material growth and its application to three-dimensional finite element analysis. *Mech Res Commun* 29 (6), 477–483.
- Ingber, D. E., Apr. 2003. Tensegrity i. cell structure and hierarchical systems biology. *Journal of Cell Science* 116 (7), 1157–1173.
- Ingber, D. E., Jun. 2008. Tensegrity-based mechanosensing from macro to micro. *Progress In Biophysics & Molecular Biology* 97 (2-3), 163–179.
- Jungbauer, S., Gao, H. J., Spatz, J. P., Kemkemer, R., Oct. 2008. Two characteristic regimes in frequency-dependent dynamic reorientation of fibroblasts on cyclically stretched substrates. *Biophysical Journal* 95 (7), 3470–3478.

- Karsaj, I., Sansour, C., Soric, J., Oct. 2009. The modelling of fibre reorientation in soft tissue. *Biomech Model Mechan* 8 (5), 359–370.
- Kratky, O., Porod, G., 1949. Röntgenuntersuchung geloster fadenmoleküle. *Recl Trav Cnim Pay B* 68 (12), 1106–1122.
- Kroon, M., Jun. 2010. A continuum mechanics framework and a constitutive model for remodelling of collagen gels and collagenous tissues. *J Mech Phys Solids* 58 (6), 918–933.
- Kuhl, E., Garikipati, K., Arruda, E. M., Gosh, K., Jul. 2005. Remodeling of biological tissue: Mechanically induced reorientation of a transversely isotropic chain network. *J Mech Phys Solids* 53 (7), 1552–1573.
- Kuhl, E., Holzapfel, G., Nov. 2007. A continuum model for remodeling in living structures. *J Mater Sci* 42 (21), 8811–8823.
- Kuhl, E., Maas, R., Himpel, G., Menzel, A., Sep. 2007. Computational modeling of arterial wall growth. *Biomech Model Mechan* 6 (5), 321–331.
- Kuhl, E., Ramm, E., de Borst, R., 2000. An anisotropic gradient damage model for quasi-brittle materials. *Comput Method Appl M* 183 (1-2), 87–103.
- Kuhl, E., Steinmann, P., Carol, I., Apr. 2001. A thermodynamically consistent approach to microplane theory. part ii. dissipation and inelastic constitutive modeling. *Int J Solids Struct* 38 (17), 2933–2952.
- Levesque, M. J., Liepsch, D., Moravec, S., Nerem, R. M., Mar. 1986. Correlation of endothelial-cell shape and wall shear-stress in a stenosed dog aorta. *Arteriosclerosis* 6 (2), 220–229.
- Machyshyn, I. M., Bovendeerd, P. H. M., van de Ven, A. A. F., Rongen, P. M. J., van de Vosse, F. N., Dec. 2010a. A model for arterial adaptation combining microstructural collagen remodeling and 3d tissue growth. *Biomechanics and Modeling In Mechanobiology* 9 (6), 671–687.
- Machyshyn, I. M., Bovendeerd, P. H. M., van de Ven, A. A. F., Rongen, P. M. J., van de Vosse, F. N., Jul. 2010b. Stability against dynamic remodeling of an arterial tissue. *Journal of Engineering Mathematics* 67 (3), 175–192.
- Marsden, J. E., Ratiu, T. S., 1999. *Introduction to Mechanics and Symmetry: A Basic Exposition of Classical Mechanical Systems*. Springer Verlag.
- Menzel, A., Mar. 2004. Modelling of anisotropic growth in biological tissues. *Biomech Model Mechan* 3 (3), 147–171.
- Menzel, A., 2007. A fibre reorientation model for orthotropic multiplicative growth. *Biomech Model Mechan* 6, 303–320.
- Menzel, A., Harrysson, M., Ristinmaa, M., 2008. Towards an orientation-distribution-based multi-scale approach for remodelling biological tissues. *Comput Meth Biomech Biomed Eng* 11 (5), 505–524.
- Menzel, A., Steinmann, P., Apr. 2003. Geometrically non-linear anisotropic inelasticity based on fictitious configurations: Application to the coupling of continuum damage and multiplicative elasto-plasticity. *Int*

- J Numer Meth Eng 56 (14), 2233–2266.
- Menzel, A., Waffenschmidt, T., Sep. 2009. A microsphere-based remodelling formulation for anisotropic biological tissues. *Phil Trans R Soc A* 367 (1902), 3499–3523.
- Miehe, C., Göktepe, S., Lulei, F., Nov. 2004. A micro-macro approach to rubber-like materials—part i: the non-affine micro-sphere model of rubber elasticity. *J Mech Phys Solids* 52 (11), 2617–2660.
- Mofrad, M. K., Kamm, R. D., 2006. *Cytoskeletal Mechanics - Models and Measurements*. Cambridge University Press.
- Narayanan, H., Verner, S. N., Mills, K. L., Kemkemer, R., Garikipati, K., May 2010. In silico estimates of the free energy rates in growing tumor spheroids. *Journal of Physics-condensed Matter* 22 (19), 194122.
- Ohashi, T., Sato, M., Jul. 2005. Remodeling of vascular endothelial cells exposed to fluid shear stress: experimental and numerical approach. *Fluid Dynamics Research* 37 (1-2), 40–59.
- Rodriguez, E. K., Hoger, A., McCulloch, A. D., Apr. 1994. Stress-dependent finite growth in soft elastic tissues. *J Biomech* 27 (4), 455–467.
- Saez, A., Buguin, A., Silberzan, P., Ladoux, B., Dec. 2005. Is the mechanical activity of epithelial cells controlled by deformations or forces? *Biophys J* 89 (6), L52–L54.
- Sander, E. A., Stylianopoulos, T., Tranquillo, R. T., Barocas, V. H., Oct. 2009. Image-based multiscale modeling predicts tissue-level and network-level fiber reorganization in stretched cell-compacted collagen gels. *PNAS* 106 (42), 17675–17680.
- Skalak, R., Dasgupta, G., Moss, M., Otten, E., Dullemeijer, P., Vilmann, H., Feb. 1982. Analytical description of growth. *J Theor Biol* 94 (3), 555–577.
- Stopak, D., Harris, A. K., 1982. Connective-tissue morphogenesis by fibroblast traction .1. tissue-culture observations. *Dev Biol* 90 (2), 383–398.
- Taber, L. A., 1995. Biomechanics of growth, remodeling, and morphogenesis. *Appl. Mech. Rev.* 48, 487–545.
- Taber, L. A., Jun. 1998. A model for aortic growth based on fluid shear and fiber stresses. *J Biomech Eng-T ASME* 120 (3), 348–354.
- Taber, L. A., Sep. 2009. Towards a unified theory for morphomechanics. *Phil Trans R Soc A* 367 (1902), 3555–3583.
- Truesdell, C., Noll, W., 2004. *The Non-Linear Field Theories of Mechanics*, 3rd Edition. Springer-Verlag.
- Vianello, M., Sep. 1996. Optimization of the stored energy and coaxiality of strain and stress in finite elasticity. *J Elasticity* 44 (3), 193–202.